Please cite this paper as J. Phys. Chem. C 2019, 123, 21083−21096

Indium doped TiO_2 photocatalysts with high temperature anatase stability

Vignesh Kumaravel [a,b],* Stephen Rhatigan [c], Snehamol Mathew [a,b], John Bartlett [a,b], Michael Nolan [c],* Steven J. Hinder [d], Preetam K. Sharma [e], Anukriti Singh [e], J. Anthony Byrne [e], John Harrison [f], Suresh C. Pillai [a,b*]

[a] *Nanotechnology and Bio-Engineering Research Group, Department of Environmental Science, School of Science, Institute of Technology Sligo, Ash Lane, Sligo, Ireland.*

[b] *Centre for Precision Engineering, Materials and Manufacturing Research (PEM), Institute of Technology Sligo, Ash Lane, Sligo, Ireland.*

[c] *Tyndall National Institute, University College Cork, Lee Maltings, Dyke Parade, Cork, Ireland.*

[d] *The Surface Analysis Laboratory, Faculty of Engineering and Physical Sciences, University of Surrey, Guildford, Surrey, United Kingdom.*

[e] *NIBEC, Ulster University, Shore Road, Newtownabbey, United Kingdom.*

[f] *InnoTech Centre, South West College, Burn Road, Cookstown, United Kingdom.*

E-mail: Kumaravel.Vignesh@itsligo.ie; Pillai.Suresh@itsligo.ie; michael.nolan@tyndall.ie

Abstract:

The thermal stability of anatase titanium dioxide (TiO_2) is a prerequisite to fabricate photocatalyst coated indoor building materials for use in antimicrobial and self-cleaning applications under normal room light illumination. Metal doping of TiO_2 is an appropriate way to control the anatase to rutile phase transition (ART) at high processing temperature. In this present work, ART of indium (In) doped TiO_2 (In-TiO_2) was investigated in detail in the range of 500 °C – 900 °C. In-TiO_2 (In mol % = 0 to 16) was synthesized *via* a modified sol-gel approach. These nanoparticles were further characterized by means of powder X-ray diffraction (XRD), Raman, photoluminescence (PL), transient photocurrent response, and X-ray photoelectron spectroscopy (XPS) techniques. XRD results showed that the anatase phase was maintained up to 64 % by 16-mol % of In doping at 800 °C of calcination temperature. XPS results revealed that the binding energies of Ti^{4+} (Ti $2p_{1/2}$ and Ti $2p_{3/2}$) were red-shifted by In doping. The influence of In doping on the electronic structure and oxygen vacancy formation of anatase TiO_2 was studied using density functional theory corrected for on-site Coulomb interactions (DFT+U). First principles results showed that the charge compensating oxygen vacancies form spontaneously at sites adjacent to the In dopant. DFT+U calculations revealed the formation of In - 5*s* states in the band gap of the anatase host. The formation of In_2O_3 at the anatase surface was also examined using a slab model of the anatase (101)

Please cite this paper as J. Phys. Chem. C 2019, 123, 21083−21096

surface modified with a nanocluster of composition In_4O_6. The formation of a reducing oxygen vacancy also has a moderate energy cost and results in charge localisation at In ions of the supported nanocluster. PL and photocurrent measurements suggested that the charge carrier recombination process in TiO_2 was reduced in the presence of In dopant. The photocatalytic activity of 2 % In-TiO_2 calcined at 700 °C is more comparable with that of pure anatase.

Keywords: Photocatalysis; Titania; Dopant: Phase stability; Nanomaterials

1. Introduction:

Titanium dioxide (TiO_2) is one of the most popular nano-materials in recent decades for its energy (solar cell [1], water splitting [2], CO_2 conversion/reduction [3]) and environmental (antimicrobial [4], self-cleaning [5], removal of toxic air/water pollutants [6, 7]) applications under UV/visible light illumination [8]. Pure TiO_2 is commonly photo-activated by UV light owing to its wide band gap (3.2 eV for anatase and 3.0 eV for rutile phase TiO_2) [7, 9]. Surface decoration [10, 11] or inclusion of appropriate materials [12-14] in TiO_2 can favour its visible light absorption for practical applications. Among the three crystalline phases of TiO_2 (such as anatase, rutile and brookite), the anatase phase shows maximum photocatalytic activity [15]. The lifetime of photo-generated charge carriers in the anatase phase is longer than that of rutile and brookite phases [16]. However, many of the commercial TiO_2 products available in the market have a mixture of ~80 % anatase and ~20 % rutile phases (*e.g.* Degussa P25) [17, 18]. It is perceived that a mixed phase composition of TiO_2 with a high percentage of anatase (more than ~ 60 %) would reduce the charge carrier recombination process and enhance the photocatalytic efficiency [19]. Therefore, TiO_2 anatase could be used as an excellent additive in the manufacturing of building materials (especially ceramic tiles sanitary ware, and glass) for indoor air purification, antimicrobial coatings and self-cleaning surfaces under normal room light illumination [20-22]. However, most of these indoor building materials are processed and manufactured at high temperatures in the range of 600 °C to 1000 °C. Usually, the anatase phase of TiO_2 is thermodynamically not stable over 600 °C, due to its low surface free energy [23-25]. At high temperatures, the photoactive TiO_2 anatase phase will be converted into the less photoactive rutile phase TiO_2. Kinetic studies have revealed that the complete transition of anatase to rutile of TiO_2 occurs in the temperature range of 673 °C - 728 °C [26]. Therefore, a thermally stable TiO_2 anatase photocatalyst is required for applications in indoor building materials [20], where the high temperature processing is used. ART temperature generally relies

on various factors, such as the synthesis method, existence of impurities/dopants, and atmosphere [23]. Doping of TiO_2 using metal/non-metal ions is one of the most convenient and cost-effective approaches to tune the band-gap energy for visible light absorption and to control the ART at high temperatures [19, 27-35]. ART of metal doped TiO_2 is influenced by the ionic radius, oxidation state and bonding nature of the dopant [23].

Recently, the ART of cobalt doped TiO_2 (Co-TiO_2) was studied at a single calcination temperature of 600 °C and a dopant (Co) concentration in the range of 0 % to 4 mol % [36]. The results revealed that ART of TiO_2 was promoted by Co doping. 4 % of Co doping in anatase produced a mixture of 78 % rutile and 22 % anatase at 600 °C. In another study, the ART of TiO_2 was studied using silicon (Si) dopant [37]. The anatase phase of TiO_2 was well maintained until 800 °C by 0.25% Si doping, with 90 % anatase and 10 % rutile. ART of TiO_2 has been shown to be promoted by tungsten (W) [38] and vanadium (V) doping [39]. The phase transformation was promoted up to 50 ppm of W^{6+} and it was inhibited thereafter (> W^{6+} 50 ppm; calcination 500 °C) [37]. 100 % rutile was formed by the addition of 6 at.% of V at a calcination temperature of 550 °C [38]. In a recent study, it was observed that the anatase phase of TiO_2 nanowires was well retained with Ti^{3+} self-doping up to a calcination temperature of 800 °C [40].

Indium (In) is a transition metal with 5*s*2 5*p*1 electronic configuration and it generally takes a +3 oxidation state. It has the tendency to create oxygen vacancies in TiO_2 [41, 42]. Indium is considered as an effective dopant for TiO_2, owing to its electronic properties and low toxicity [42, 43]. Doping of such metal ions into TiO_2 would be beneficial to enrich the photocatalytic activity [44] *via* inhibiting the photo-generated charge-carrier recombination and promoting the adsorption of microbes/pollutants on the active sites of photocatalyst [42, 45]. In doped TiO_2 was studied for the photocatalytic reduction of carbon dioxide (CO_2) under UV light irradiation [42, 46]. The dopant concentration was examined in the range of 0 wt % to 20 wt % and the calcination temperature was fixed at 500 °C for 5 h. The results revealed that no phase transition occurred in In-TiO_2 during this calcination step. The CO_2 reduction efficiency was increased significantly for the In-doped samples as compared to pure TiO_2. The efficiency of 10 wt % In-TiO_2 was 7.9 fold higher than that of un-doped TiO_2. Wang *et al.* [47] reported the visible light assisted photocatalytic efficiency of In-TiO_2 for the degradation of 4-chlorophenol. In was studied in the range of 3 mol % to 15 mol % and the calcination temperature was fixed at 450 °C for 2.5 h. These results suggest that the electron-

hole recombination was minimized and the photocatalytic activity was enhanced by In doping, which helps to stabilize the anatase phase.

First principle studies of In-doped TiO_2 are sparse in the literature. Wang *et al.* reported the visible light assisted photocatalytic activity for In-TiO_2 anatase, which was attributed to the presence of a surface species, O-In-Cl_x (x = 1 or 2) [47]. This species introduced a surface state energy level at 0.3 eV below the TiO_2 CB. This work was followed with a study of TiO_2 co-modified with N and In, which included DFT calculations of the electronic band structure and density of states (DOS) for In-TiO_2 [48]. While details of the exact computational set-up are lacking, the authors reported that In-derived states emerge at 0.5 eV below the TiO_2 CB, in their generalized gradient approximation (GGA) calculations. Charge compensation *via* oxygen vacancy formation in In-TiO_2 rutile was previously studied using standard DFT, DFT+U and hybrid DFT [49]. A recent GGA study presented an analysis of the band structure and DOS for stoichiometric and charge compensated In-TiO_2 anatase [50]. The details regarding the oxidation states, oxygen vacancy formation, reduction and charge localization were not provided.

There are no comprehensive or systematic studies available in the literature on the ART of In-TiO_2. In this paper, we study the ART of In doped TiO_2 (In-TiO_2) nanoparticles calcined for 2 h temperatures in the range of 500 °C to 900 °C; this includes temperature at which undoped anatase transforms to rutile. In-TiO_2 was synthesized using a sol-gel technique with different mol percentages of In (0 %, 2 %, 4 %, 8 % and16 %). The calculations of the energetics involved in the formation of charge compensating and subsequent oxygen vacancies, the DOS of the ground state and reduced system, and charge localization after reducing oxygen vacancy formation were investigated through DFT. ART was studied in detail by DFT, XRD, XPS, PL and Raman spectroscopy techniques. The anatase phase of TiO_2 is well maintained by the In dopant till 800 °C. The charge carrier recombination is highly minimized *via* the formation of In 5*s* states between the conduction band (CB) and valance band (VB) of TiO_2.

The formation energies of charge compensating and reducing oxygen vacancies in In-TiO_2 were computed through the DFT model. There is no impact on the bandgap due to In-doping in the charge compensated system, however, after localisation of charge in the vicinity of the In-dopant after the formation of a reducing oxygen vacancy, occupied states emerge in the bandgap of TiO_2. A model of a nanocluster of composition In_4O_6 at the anatase

(101) surface (denoted In_4O_6-a101) was considered to examine the impact of In_2O_3 formation at high calcination temperatures.

2. Materials and methods

All the materials used were of analytical grade and they were used as received without further purification. Double distilled water was used in the experiments.

2.1. Synthesis of indium doped TiO_2 (In-TiO_2):

2 mol % In-TiO_2 was synthesized through a sol-gel technique as follows: In a typical experiment, 38 ml of titanium isopropoxide (TTIP) was taken in 200 ml of isopropanol and the mixture was stirred for 15 min at RTP (solution A). 0.786 g of indium nitrate ($In(NO_3)_3.xH_2O$) was dissolved separately in 200 ml of double distilled water (solution B) at RTP. Then, solution B was added drop wisely into solution A under constant stirring for 30 min. The resulting gel was dried in an oven at 100 °C for 24 h. Afterwards, the powders were calcined in a muffle furnace at various temperatures (500 °C, 600 °C, 700 °C, 750 °C, 800 °C, 850 °C and 900 °C) at a ramp rate of 10 °C/min for 2 h. The samples were synthesized using various mol % of In. The as-synthesized samples such as such as 0 mol % In-TiO_2, 2 mol % In-TiO_2, 4 mol % In-TiO_2, 8 mol % In-TiO_2 and 16 mol % In-TiO_2 were labelled as TiIn-0, TiIn-2, TiIn-4, TiIn-8 and TiIn-16, respectively. Pure TiO_2 was synthesized using the same procedure without the addition of In precursor.

2.2. Density functional theory (DFT) studies:

DFT calculations were carried out using the VASP5.4 [51, 52] code with projector augmented wave [53, 54] (PAW) potentials to account for the core-valence interaction. Titanium (Ti) is described with 12 valence electrons, oxygen (O) with six and indium (In) with 13. The energy cut-off for the plane wave basis set is 400 eV and the convergence criterion for electronic relaxations is 10^{-5} eV. Indium (In) was substitutionally doped onto two Ti sites in a $(2 \times 2 \times 1)$ anatase supercell, to give a dopant concentration of 12.5 at.%. A previous study revealed that interstitial sites have higher formation energies relative to substitutional doping [49] . Therefore, interstitial sites were not considered in this study. The bulk lattice parameters of the anatase unit cell were computed as: a = 3.791 Å and b = 9.584 Å.

After substituting two In ions for Ti, two relaxations were performed; the first in which only the ionic positions were relaxed (supercell with dimensions fixed to those of pure anatase) and in the second a full relaxation of both ionic positions and supercell parameters. After the latter relaxation, the lattice dimensions expand in response to In-doping; the unit cell parameters of In-doped TiO_2 are a = 3.830 Å and c = 9.999 Å, corresponding to an increase of 1% and 4%, respectively. These changes in the lattice dimensions are small and any impact on the computed properties is expected to be negligible.

A $(4 \times 4 \times 4)$ k-point sampling grid was used and structures were relaxed until forces were less than 0.01 eV/Å. Calculations were spin-polarized and no symmetry constraints were imposed. The calculations include an on-site Hubbard correction (DFT+U) [55, 56] to describe the partially filled Ti 3*d* state; U = 4.5 eV is applied to Ti 3*d* states, with this choice for U informed by previous studies [57-61].

Oxygen vacancy formation is the mechanism of charge compensation in response to the substitution of In^{3+} for Ti^{4+} ions. To study this, multiple oxygen sites of the most stable In-doped structure were considered and the energy of formation was calculated via:

$$E^{vac} = E\left(In_xTi_{1-x}O_{2-y}\right) + 1/2E(O_2) - E(In_xTi_{1-x}O_2) \quad (1)$$

where $E\left(In_xTi_{1-x}O_{2-y}\right)$ is the total energy of In-doped TiO_2 with a charge compensating oxygen vacancy and $E\left(In_xTi_{1-x}O_2\right)$ is the total energy of In-doped TiO_2. The formation energy is referenced to half the total energy of O_2. A negative value for E^{vac} indicates that the vacancy will form spontaneously at 0 K. The energy cost to produce a second, reducing oxygen vacancy is computed similarly using:

$$E^{vac} = E\left(In_xTi_{1-x}O_{2-y'}\right) + 1/2E(O_2) - E\left(In_xTi_{1-x}O_{2-y}\right) \quad (2)$$

where $E\left(In_xTi_{1-x}O_{2-y'}\right)$ is the total energy of In doped TiO_2 with two oxygen vacancies. The oxidation states were analysed through Bader charge analysis [62] and computed spin magnetizations

To examine the presence of In_2O_3, a nanocluster of In_4O_6 composition at the anatase (101) surface (denoted as In_4O_6-a101) was considered. The anatase (101) support is modelled as a 12 atomic layer thick slab with a (1×4) surface expansion and a vacuum gap of 20 Å. For these calculations, k-point sampling was performed at the gamma-point and the remaining computational parameters are consistent with those described above for the bulk

calculations. The adsorption energy of the In_4O_6 nanocluster at the anatase (101) surface is computed as follows:

$$E^{ads} = E(In_4O_6\text{-a101}) - E(\text{a101}) - E(In_4O_6) \quad (3)$$

where the first, second and third terms on the right-hand side refer to the total energy of nanocluster-surface composite, bare anatase (101) and the gas phase In_4O_6 nanocluster, respectively. The formation energies of a single and reducing oxygen vacancy in the supported nanocluster were computed using the following equation:

$$E^{vac} = E(In_4O_5\text{-a101}) + 1/2E(O_2) - E(In_4O_6\text{-a101}) \quad (4)$$

2.3. Characterization:

ART and the TiO_2 crystalline phases were studied with the help of X-ray diffraction (XRD) using Cu Kα radiation (λ= 0.15418 nm) in the 2θ range of 10 °- 80 ° in a Siemens D500 XRD instrument. The percentages of TiO_2 anatase and rutile were calculated though the Spurr equation [25, 63]:

$$F_R = \frac{1}{1+0.8[I_A(101)/I_R(110)]} \quad (5)$$

Where F_R is the quantity of rutile phase; $I_A(101)$ and $I_R(110)$ are the intensities of anatase and rutile peaks, respectively. The average crystallite size was determined using the Scherrer equation [11, 64]. ART was also analyzed *via* Raman spectroscopy (Horiba Jobin Yvan LabRAM HR 800) with a grating of 300 gr/mm. The acquisition time of Raman analysis was 3 seconds. The oxidation state of elements and the bonding interactions of In-TiO_2 were examined by an X-ray photoelectron spectroscopy (XPS; ThermoFisher Scientific Instruments (East Grinstead, UK) with K-Alpha$^+$ spectrometer). The charge carrier recombination process was studied in terms of photoluminescence (PL) spectroscopy with an excitation wavelength of 350 nm. The photocatalytic activity (0.5 g/L) was evaluated using 0.5 g/L of nanoparticles for hydrogen (H_2) production in a 230 ml stainless steel reactor with a quartz window. The experiments were carried out using 115 ml of double distilled water under simulated solar light irradiation (300 W ozone free Xe lamp). Glycerol (10 %) was used as a sacrificial agent. H_2 gas was analysed through an Agilent gas chromatography (GC) with thermal conductivity detector (TCD) and flame ionization detector (FID). Carboxen-1000 packed column was used in the GC.

2.4. Photocurrent measurements:

The nanoparticles were sonicated in methanol followed by spray coating on a clean titanium foil [65]. The spray-coated samples were annealed at 400 °C (ramp 2 ^{o}C min^{-1} up, 2 ^{o}C min^{-1} down) to enhance the adhesion and inter-particle cohesion. The final loading of the samples was 1 mg.cm^{-2} on a 2 cm^{2} photoactive area. Electrical contact to the Ti foil was made with copper wire using silver epoxy. The contact and any are not coated with TiO_2 were insulated by SU8 (MicroChem) photoresist. The photocurrent measurements were performed using an Autolab PG30 electrochemical workstation coupled with the irradiation source of 450 W Xe lamp. The measurements under irradiated and dark conditions were obtained using a Uniblitz chopper in front of the irradiation source. Electrochemical measurements were performed in a three-electrode cell using platinum mesh as counter electrode and saturated calomel as reference electrode. The electrochemical cell was equipped with a quartz window to irradiate the working electrode. 0.1 M perchloric acid was used as an electrolyte and all potentials are reported relative to saturated calomel electrode (SCE). The photocurrent responses were measured at a fixed potential of +1.0 V.

3. Results and Discussion

The impact of In doping on the ART of TiO_2 samples synthesized at various calcination temperatures: 500 °C, 600 °C, 700 °C, 750 °C, 800 °C, 850 °C and 900 °C, were examined by XRD. The changes in the lattice parameters of TiO_2 by In doping was studied by Raman spectroscopy. The bonding interactions, formation of new energy levels and oxygen vacancies of In-TiO_2 framework were investigated through DFT and XPS. The results were compared with pure TiO_2 anatase and rutile.

Density functional theory (DFT) calculations:

Fig. 1 (a) shows the $(2 \times 2 \times 1)$ anatase supercell and the local atomic structure in the vicinity of In dopants. The most favourable dopant configuration is that in which both In ions are incorporated at Ti sites in the same Ti (001) sub-lattice plane, as shown in Fig. 1. However, a number of other configurations were very close in energy (within 0.2-6.0 meV per TiO_2 unit). The geometry about the dopant sites is symmetric. In-O distances are 2.22 Å for apical (O_{ap}) and 2.03 Å for equatorial (O_{eq}) oxygen sites. These values compare with values of 2.00 Å and 1.94 Å for equivalent Ti-O distances in un-doped anatase. Replacing two Ti^{4+} with two In^{3+} ions means a deficit of two valence electrons and, in this

computational set up, the excess charge is distributed over all O ions in the supercell as shown in Fig.1 (b).

Applying the GGA+U to the O 2*p* states, with U = 5.5 eV, yields a solution in which the excess charge is distributed only over the O ions found at apical positions relative to the In-dopants. Bader charges for these sites decrease from 7.2 to 7.1 electrons and computed spin magnetizations are 0.3 μ_B. After this localization of charge each In-O_{ap} distance increases to 2.24 Å. If we now distort the initial structure about the dopant sites to break the symmetry, the geometry relaxes to an asymmetric solution, which is more favourable than the symmetric solution by 0.34 eV (Fig. 1(c)). In this configuration, the excess charge localizes predominantly on a single apical oxygen site neighbouring each In-dopant. The computed Bader charges decrease from 7.2 to 6.8 electrons and the computed spin magnetizations are 0.7 μ_B for these oxygen sites, indicating the formation of oxygen polarons (O^-) [30, 49]. It is this localization of charge which produces the asymmetric geometry distortion. In-O^- distances are 2.31 Å, In-O_{ap} distances are 2.19 Å and In-O_{eq} distances are 2.02-2.05 Å.

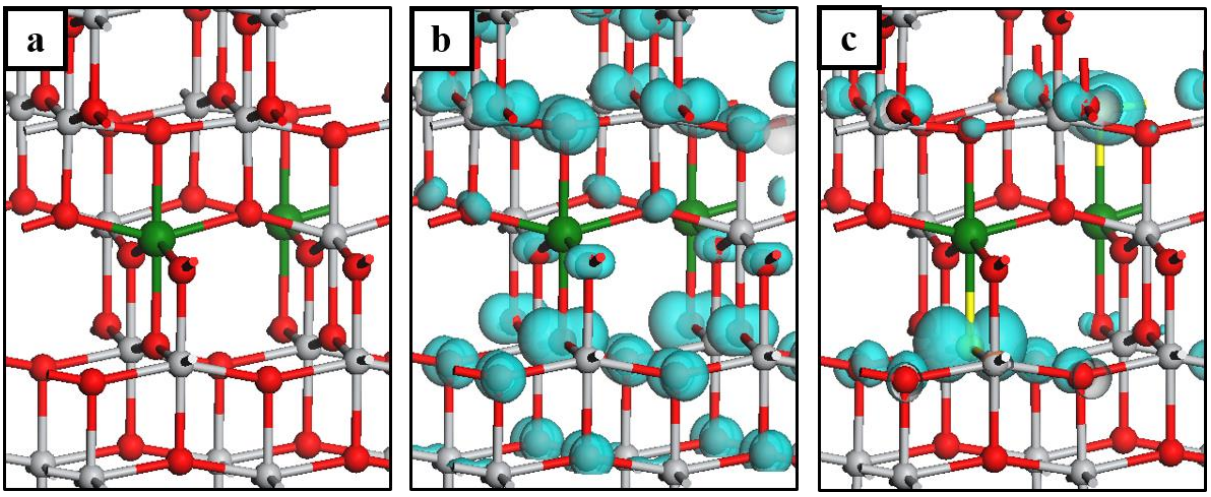

Fig. 1 Panel **(a)** shows the positions of In-dopant in the anatase lattice. Panel **(b)** shows the excess spin density plot for the computational set up with no +U correction on the O 2*p* states. Panel **(c)** shows the excess spin density plot for the computational set up with an additional +U correction on the O 2*p* states and for which the geometry was distorted from symmetry prior to relaxation. Ti is represented by grey spheres, O by red spheres, In by green spheres and the oxygen hole polarons (O^-) are highlighted in yellow. The blue iso-surface encloses spin densities up to 0.02 electrons/$Å^2$.

Oxygen vacancy formation is the mechanism by which the charge mismatch that results from substitution of Ti ions with lower valent In-dopants is compensated [45]. The computed

formation energies for a single compensating oxygen vacancy were in the range -0.24 eV to +0.84 eV, depending on the O site considered. The negative oxygen vacancy formation energy confirms that the charge compensated structure is favourable. Formation of the most stable vacancy was more favourable than the next most stable by 0.12 eV and the resulting geometry is shown in the top panels of Fig. 2. The most stable oxygen vacancy in the fully relaxed structure has a formation energy of -0.11 eV, which shows that oxygen vacancy formation takes place to charge balance the In dopant. The removed O ion was in an equatorial position relative to the In-dopant and, after formation of a vacancy at this site, the neighbouring Ti and In sites are five-fold coordinated. The Ti ions move off their lattice sites by 0.2 Å away from the vacancy and the Ti-O distances opposite the vacancy are shortened by 0.10-0.14 Å relative to the bond lengths prior to vacancy formation. The In-dopant moves 0.2 Å closer to the vacancy and, since there are no oxygen polarons after charge compensation, the In-O_{ap} distances are shortened to 2.09 and 2.15 Å. The remaining In-O_{eq} distances are 2.00-2.08 Å. For the second In-dopant, away from the vacancy site, the In-O_{ap} distances are 2.14 and 2.19 Å and the In-O_{eq} distances are 2.02-2.12 Å.

Formation of a second, reducing oxygen vacancy, which is implicated in the ART, was considered, and the computed formation energies lie in the range of 3.80-5.84 eV. Energies at the lower end of this range mean that the In-doped system is reducible, with moderate energy costs, and, given the elevated preparation temperatures, such reducing oxygen vacancies will be expected to form. In the fully relaxed super cell, the most stable reducing oxygen vacancy forms with an energy cost of 4.41 eV. While this cost is larger than that in the fixed supercell, it is still moderate when compared with an energy cost of 5.2 eV to produce a single, reducing oxygen vacancy in the $(2 \times 2 \times 1)$ un-doped anatase supercell, computed with the same input parameters. The most stable site for the formation of a reducing vacancy is an equatorial site of the second In-dopant, as shown in the bottom panels of Fig. 2. In this instance, the In-dopants move 0.4 Å off the lattice site and towards the vacancy sites, while the Ti ions move 0.1-0.3 Å outwards from the vacancy sites. The geometry in the vicinity of both In-dopant is similar; the In-O_{ap} distances are 2.18 Å, two In-O_{eq} distances are 2.10 Å and the third, opposite the vacancy, is longer, at 2.22 Å.

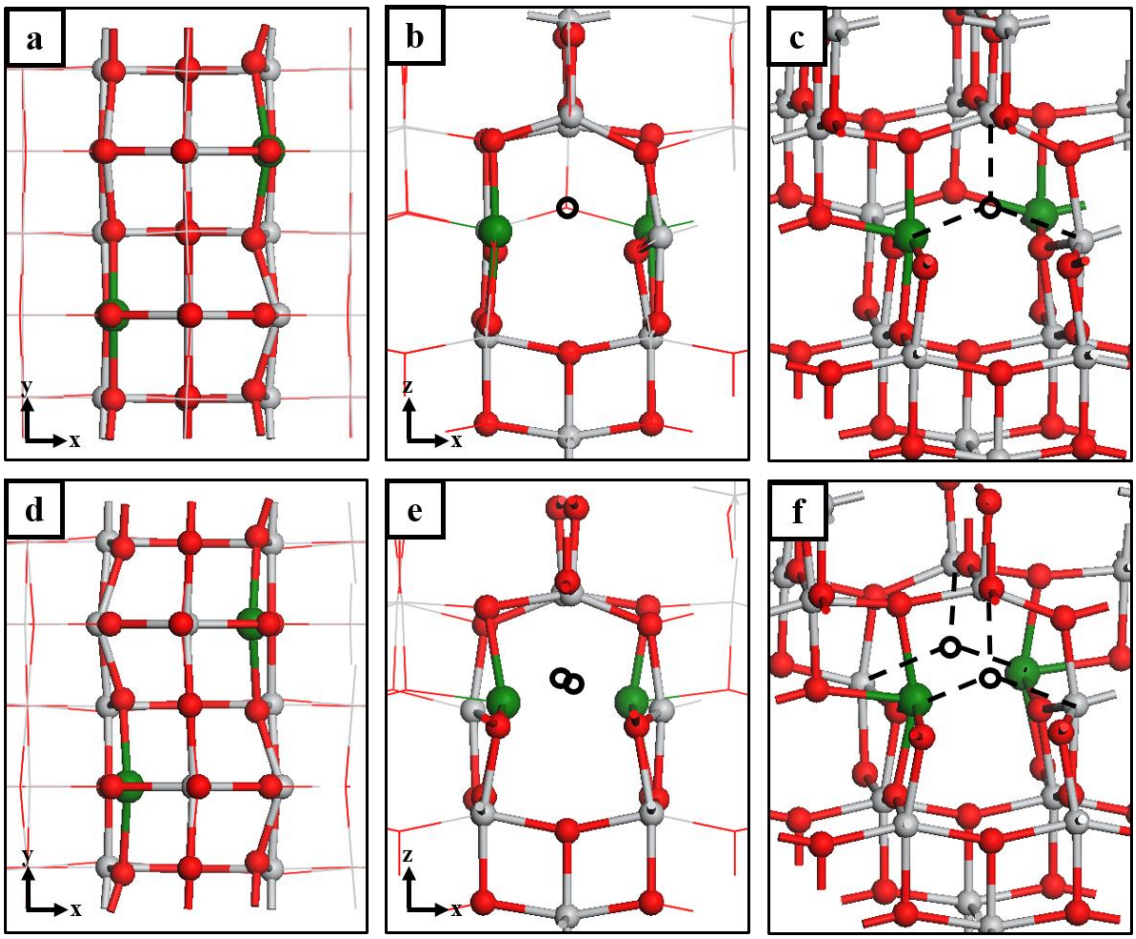

Fig. 2. The top panels display distortions to the lattice of In-doped anatase TiO_2 in response to the charge compensating oxygen vacancy. Bottom panels show the atomic structure after formation of a second, reducing oxygen vacancy. The xy-plane geometry, shown in **(a)** and **(d)**, and the xz-plane geometry, shown in **(b)** and **(e)**, highlight the movement of the In-dopants towards the vacancy sites and the movement of Ti ions away from the vacancies, represented by black circles. Panel **(c)** and **(f)** indicate the cations to which the removed oxygen ions were bound.

With two oxygen vacancies in In-doped anatase, there is an excess of two electrons and the computed Bader charges reveal that some of this charge is distributed over the cations to which the removed oxygen ions were bound. For the In-dopants the Bader charges increase from 11.0 to 11.5 electrons and these sites have spin magnetizations of 0.2 μ_B. For the Ti sites, the Bader charges increase from 9.6 to 9.7/9.8 electrons, where the vacancy sits in an equatorial/apical position relative to the Ti ion. Similarly, these Ti sites have computed spin

magnetizations of 0.1/0.2 μ_B. These values, in particular those for the spin magnetization, indicate that the excess electrons are not fully localized. The excess spin density plots in Fig. 3 show that the charge is distributed over site of the removed oxygen atom, similar to an F-centre, and with some localisation onto neighbouring Ti and In sites.

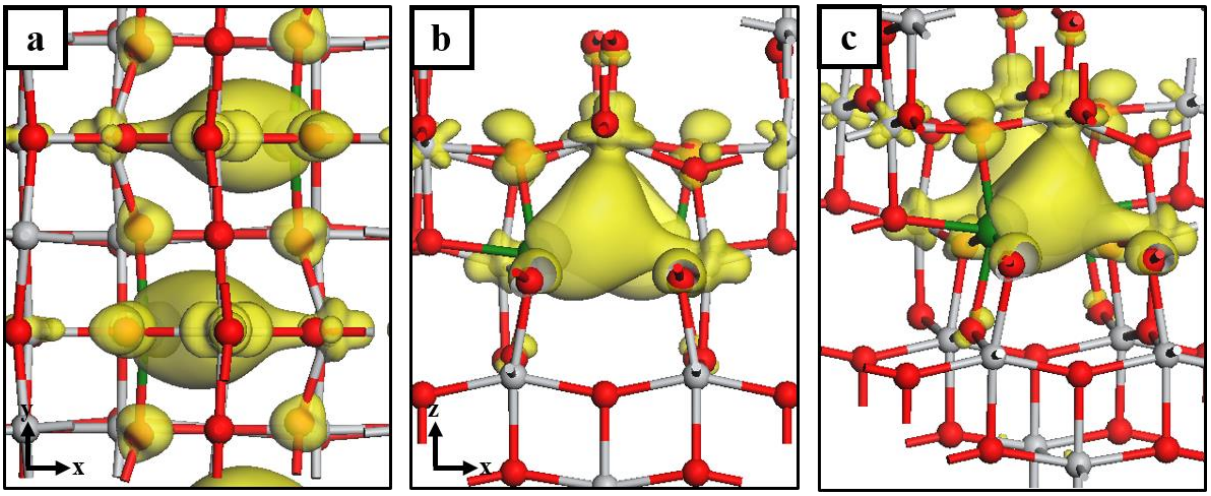

Fig. 3 Excess spin density plot showing the localization of electrons after formation of a second, reducing oxygen vacancy in In-doped anatase TiO_2. Panels **(a)**, **(b)** and **(c)** display the geometry in the xy-plane, xz-plane and from an angled view. The yellow isosurface encloses spin densities up to 0.02 electrons/Å^2

The energy cost to produce a third oxygen vacancy is in the range of 5.1-5.9 eV, depending on the vacancy site. This can be compared with an energy cost of 5.2 eV to produce a single, reducing oxygen vacancy in the $(2 \times 2 \times 1)$ un-doped anatase supercell, computed with the same input parameters. Thus, In doping can lead to less favourable vacancy formation, although the precise details of the ART mechanism is reported to be more complex than oxygen vacancy formation [66, 67].

The projected electronic density of states (PEDOS) plots are shown in Fig. 4 for (a) un-doped anatase, (c) the ground state In-doped system, with a single, compensating oxygen vacancy, and (d) the reduced In-doped system, with two oxygen vacancies. For reference, the computed PEDOS for In-doped anatase prior to charge compensation is shown in Fig. 4 (b). However, as this does not represent a physical system, due to oxygen vacancies forming spontaneously at 0 K, it is included only for completeness.

For the ground state In-doped system, the PEDOS plot in Fig. 4 (c) yields a band gap of 2.44 eV, which compares with a value of 2.70 eV for the un-doped system. For the PEDOS

plot in Fig. 4 (d), the titania-derived band gap is 2.49 eV and states emerge in this gap which arise due to cation reduction in response to formation of a second, reducing oxygen vacancy and are associated with the spin density as shown in Fig. 3. The first peak emerges at 1.59 eV above the valence band max (VBM) of the TiO_2 host and is associated with the singly-occupied, 5*s* orbitals of the In-dopants. The next states lie higher in energy, at 2.17 eV above the TiO_2 VBM, and are derived from the empty 5*s* orbitals of the In-dopants.

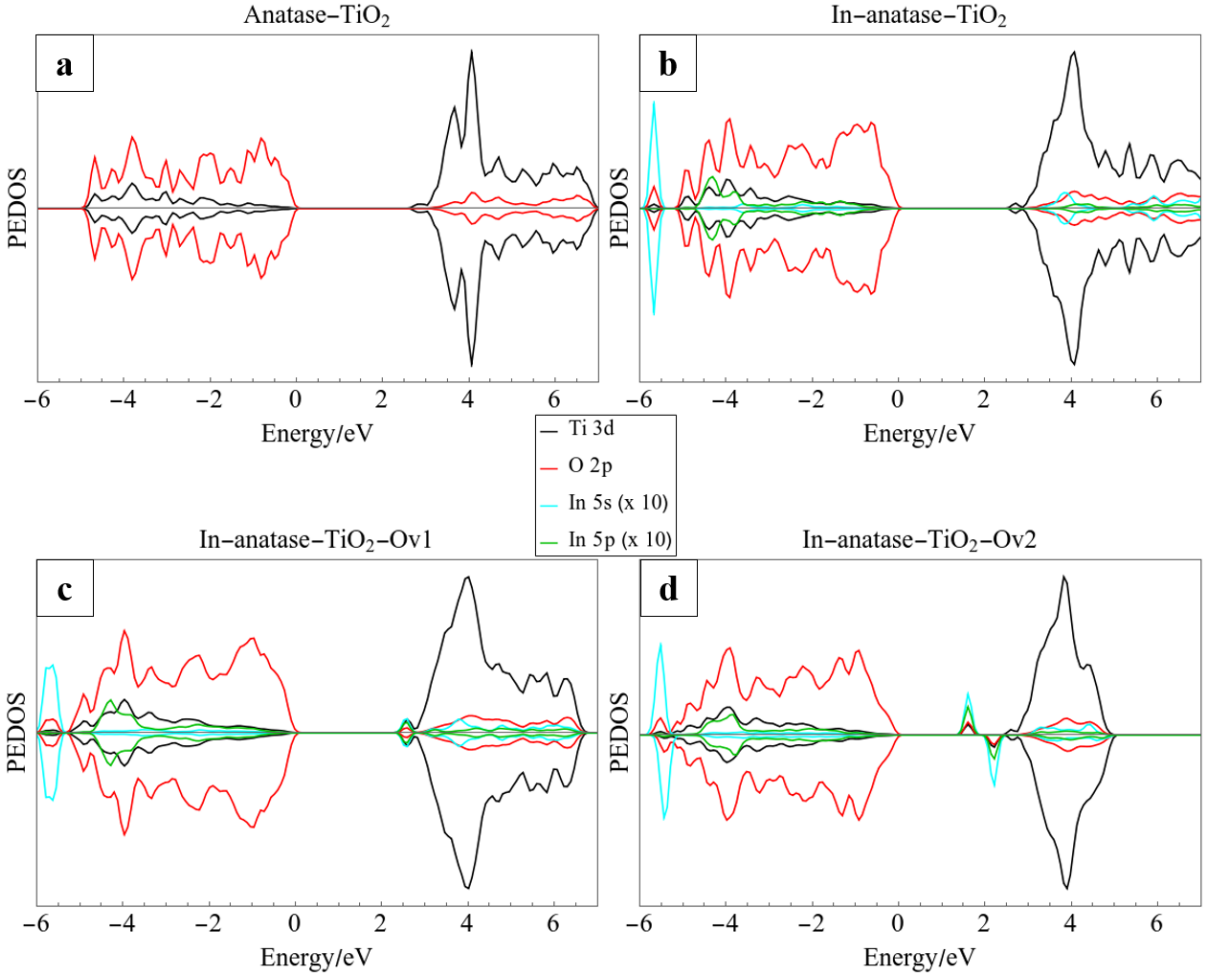

Fig. 4. Projected electronic density of states (PEDOS) computed for **(a)** undoped anatase and **(b)** In-doped anatase with no oxygen vacancies are included for reference. The PEDOS of the ground state structure, with a single, charge compensating oxygen vacancy and the reduced system with two oxygen vacancies are shown in panels **(c)** and **(d)**.

To examine the influence of In_2O_3 on the properties of In-doped anatase, a model of an In_4O_6 nanocluster modifying the anatase (101) surface (In_4O_6-a101) was implemented. The computed adsorption energy is -3.42 eV, showing that the cluster-surface interaction is

favourable. However, at high calcination temperatures, it is possible that the nanoclusters will desorb or migrate and aggregate at the surface to form larger nanoclusters. The latter eventuality would lead to enhanced In_2O_3 signals in the XRD spectrum.

The relaxed structure of stoichiometric In_4O_6-a101 is shown in Fig. 5 (a). In_4O_6 binds to the surface *via* the formation of three In-O and three Ti-O bonds. Three In ions are four-fold coordinated and the fourth In ion is three-fold coordinated; In-O bond lengths are in the range 1.96-2.19 Å. Three cluster O ions are three-fold coordinated and the remaining three O ions are doubly coordinated. The interfacial Ti-O distance is 1.86-2.08 Å. The computed Bader charges for In ions in the stoichiometric cluster are 11.2-11.3 electrons, to which we ascribe an oxidation state of In^{3+}.

The formation energy for the most stable oxygen vacancy in the supported In_4O_6 nanocluster is computed as 2.19 eV. The relaxed structure of In_4O_5-a101 is shown in Fig. 5 (b). In this configuration, there are seven interfacial bonds (four In-O and three Ti-O bonds); In-O distances are in the range 2.06-2.36 Å and interfacial Ti-O distances are 1.88-1.96 Å. Two electrons are released after the formation of a neutral oxygen vacancy and these localise at In ions, as shown in the excess spin density plot (Fig. 5 (b)); the Bader charges for these sites increase from 11.2 and 11.3 electrons to 11.8 electrons. Electron localisation is further confirmed by computed spin magnetisations of 0.3 and 0.4 μ_B. Based on these results, and given the moderate oxygen vacancy formation energy, should In_2O_3 form at the anatase surface, In ions will be present in a mixture of oxidation states. In particular, localisation of charge at In ions at the surface will contribute to the photocatalytic activity.

The PEDOS of In_4O_6-a101 and In_4O_5-a101 are shown in Fig. 6 (a) and 6 (b), respectively. For In_4O_6-a101, states derived from cluster O ions extend to 0.2 eV above the VBM of titania. In addition, In-derived states emerge in the bandgap at 0.5 eV below the CBM. For the reduced system (In_4O_5-a101), cluster O 2*p*-derived states persist to 0.4 eV above the VBM and additional In-derived occupied states emerge in the titania bandgap at 1.3 eV above the VBM. For both stoichiometric In_4O_6-a101 and reduced In_4O_5-a101 systems, these features suggest a red-shift in the light absorption edge and could enhance the lifetime of charge carriers on the photocatalyst surface as compared to bare anatase (101).

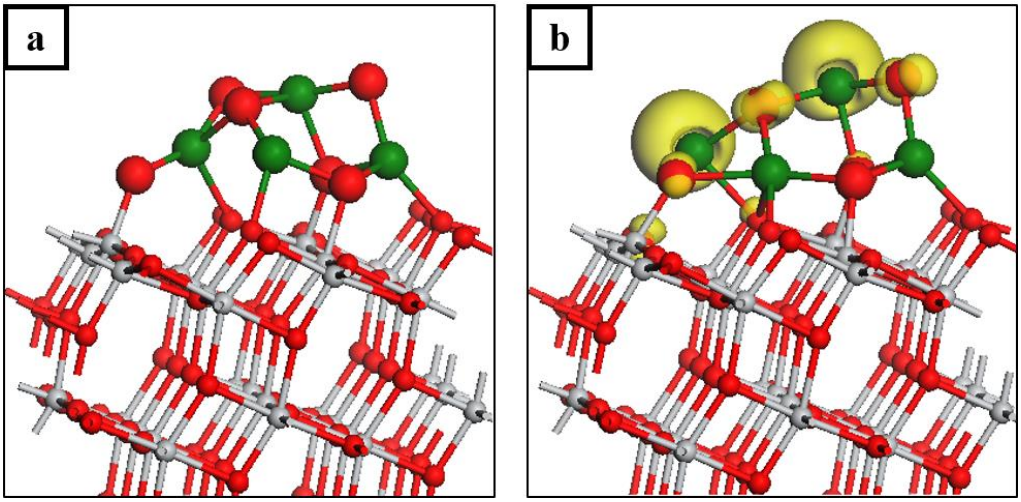

Fig. 5. The relaxed atomic structure of **(a)** stoichiometric In_4O_6-a101 and **(b)** reduced In_4O_5-a101. The yellow iso-surface encloses spin densities up to 0.02 electrons/Å^2.

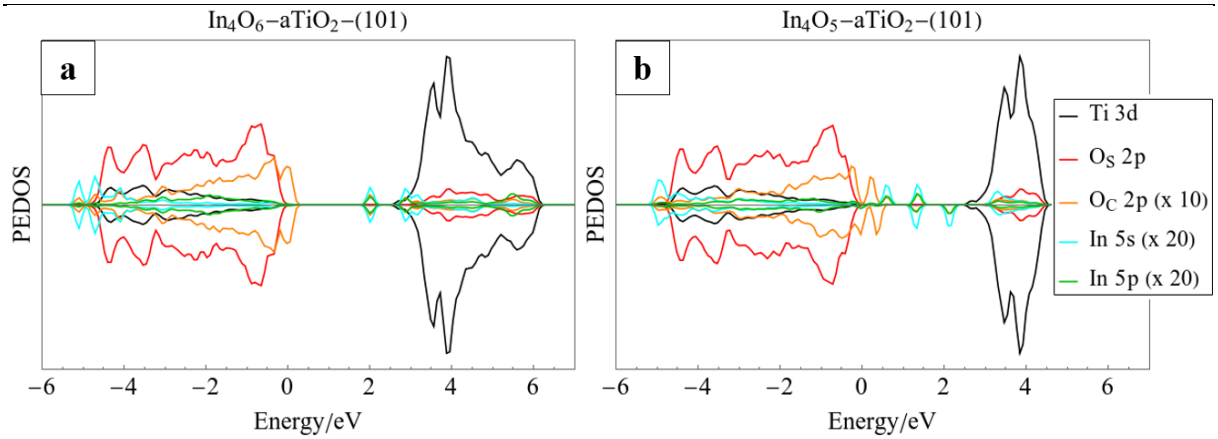

Fig. 6. Projected electronic density of states (PEDOS) computed for **(a)** stoichiometric In_4O_6-a101 and **(b)** reduced In_4O_5-a101.

X-ray diffraction:

XRD patterns of pristine TiO_2 and In-TiO_2 calcined at 500 °C, 700 °C, 800 °C and 900 °C are shown in Fig. 7. The percentages of anatase and rutile phases in In-TiO_2 samples are given in Table 1. At 500 °C, the diffraction peaks of all samples are matched with the anatase phase TiO_2. Undoped TiO_2 is almost transformed into the rutile phase (90 % rutile and 10 % anatase) when the calcination temperature is increased to 600 °C. Nevertheless, the anatase phase is well retained for In-TiO_2 samples up to 700 °C. A mixture of anatase and rutile phases is formed for In-TiO_2 samples at 800 °C (Fig. 8 (a)). Moreover, some additional peaks also appear, due to the formation of indium trioxide (In_2O_3). The peak intensities for indium oxide are increased with increase of In dopant concentration. All samples completely

transform to rutile at 900 °C calcination temperature. For In-TiO_2 (especially at 600 °C, 700 °C and 800 °C), the (101) anatase peak is slightly shifted after In doping, suggesting the substitution of Ti^{4+} ions by In^{3+} ions in the crystal lattice of TiO_2 [68, 69]. This is ascribed to the fact that the lattice parameters and cell volume of In-TiO_2 being larger than pure anatase TiO_2. TiIn-2 (at 800 °C) and TiIn-16 (at 800 °C) samples showed remarkable anatase and rutile percentages with respect to commercial TiO_2 p25. The crystallite size of TiO_2 is gradually reduced with increase of In content (Fig. 8 (b)). This is ascribed to the crystallization and agglomeration of TiO_2 being retarded by In doping [70-72]. TiO_2 crystal framework may be stressed by the substitution of Ti^{4+} or superficial O_2 ions by In^{3+} ions and the O-Ti-OH surface bonds are affected by In doping[47]. Wang *et al.* [48] suggested that the increase of In concentration (from 5 to 10 %) in TiO_2 favours the rutile formation in small amounts at the calcination temperature of 450 °C. However, in this present work, the rutile formation is highly restricted up to 700 °C by In doping. Hinojosa-Reyes *et al.* [70] found that the anatase phase could be retained up to 1000 °C by In doping with a decreased calcination time of 30 min. These results suggest that the calcination time can also play a role in the ART of In-TiO_2. Moreover, the calcination time of 2 h is sufficient for the complete transformation of anatase to rutile. The lattice constants (*a* and *c*) and cell volume (*V*) were calculated for the samples (0 % In-TiO_2 @500 °C, 2 % In-TiO_2 @750 °C, 4% In-TiO_2 @750 °C and 16 % In-TiO_2 @800 °C) with high anatase content (Table S1). The cell volume (from 135.4 to 135.8) and lattice constant '*c*' (from 9.48 to 9.50) of pure TiO_2 anatase are slightly increased after doping with In. The results revealed that the impact of In doping on the anatase lattice parameters are negligible.

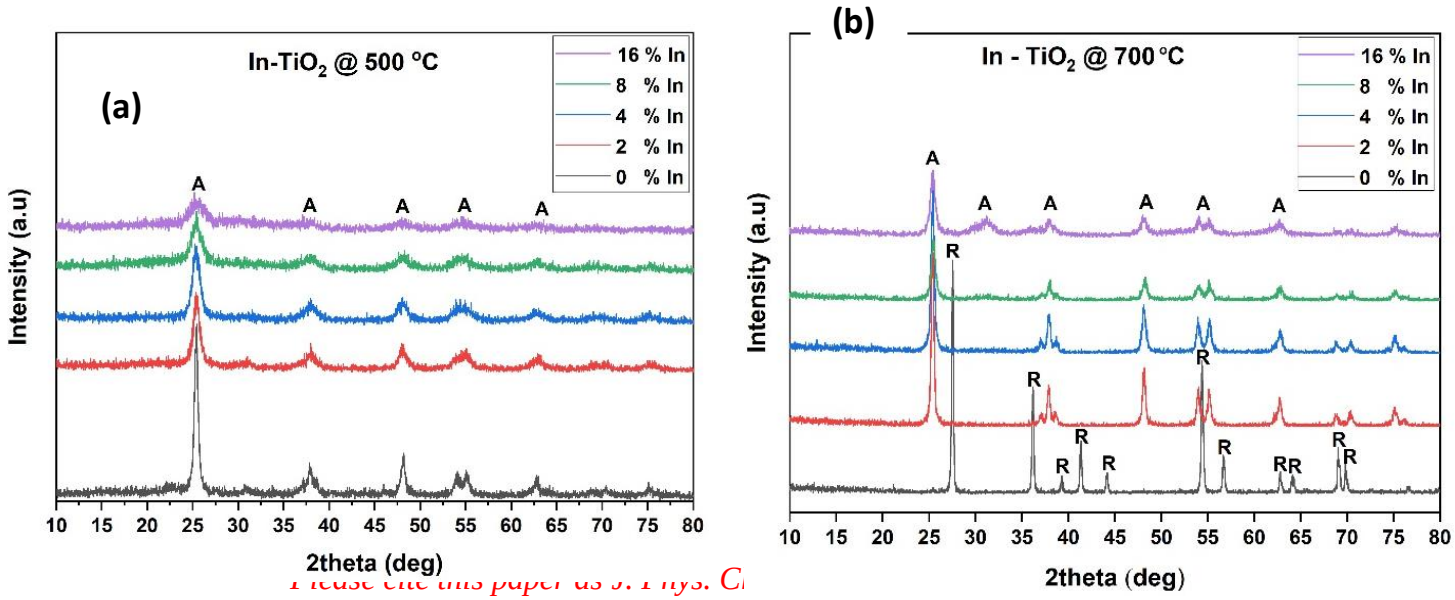

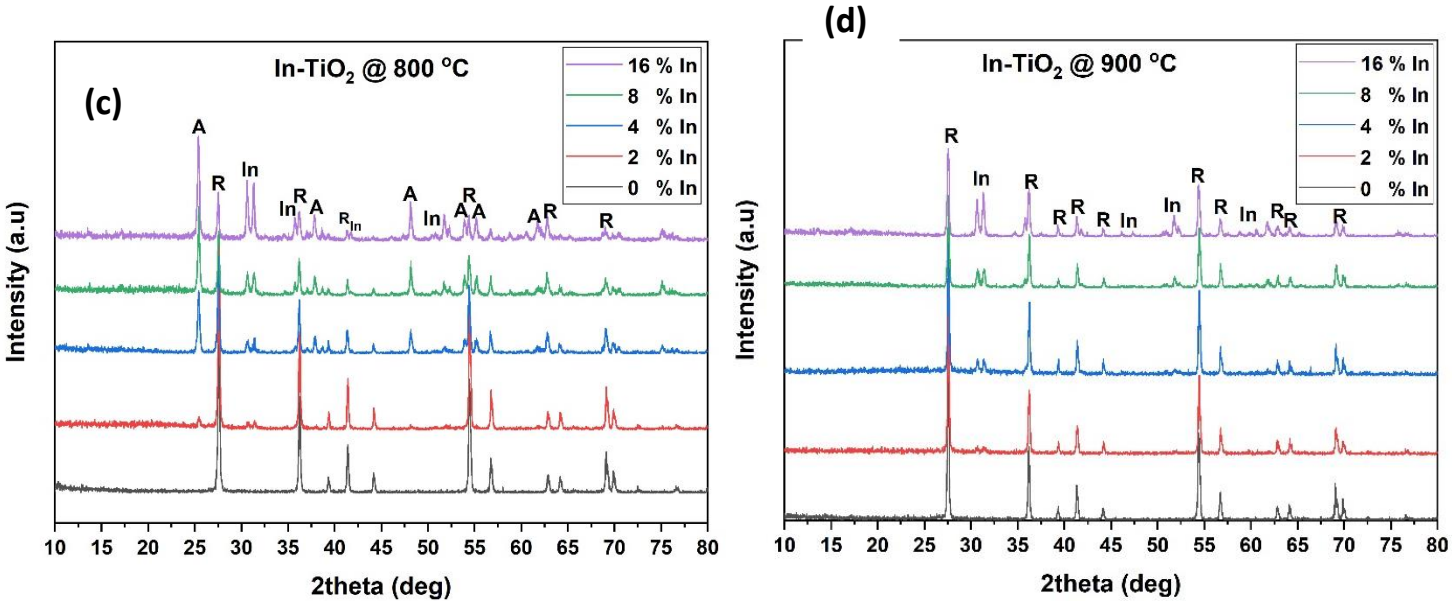

Fig. 7. XRD patterns of In-TiO_2 calcined at (a) 500 °C (b) 700 °C (c) 800 °C and (d) 900 °C

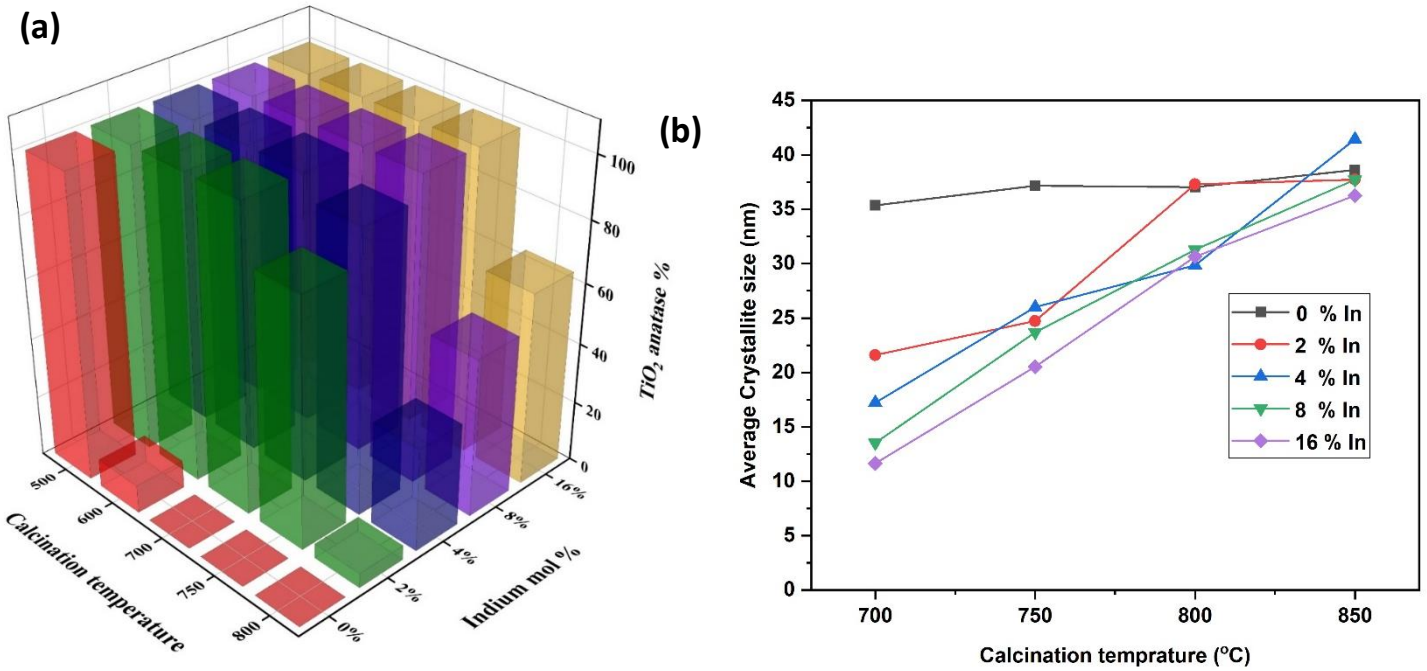

Fig. 8. (a) The anatase phase percentage of In-TiO_2 samples at various calcination temperature (b) the average crystallite size of In-TiO_2 at various calcination temperatures

Table. 1. Anatase and rutile percentages of In-TiO_2 samples at various calcination temperatures

Samples	500 °C		600 °C		700 °C		750 °C		800 °C		850 °C		900 °C	
	A	R	A	R	A	R	A	R	A	R	A	R	A	R
0 % In-TiO_2	100	-	9.31	90.69	-	100	-	100	-	100	-	100	-	100
2 % In-TiO_2	100	-	100	-	100	-	81.94	18.06	4.87	95.13	-	100	-	100
4 % In-TiO_2	100	-	100	-	100	-	92.58	7.42	34.27	65.73	-	100	-	100
8 % In-TiO_2	100	-	100	-	100	-	100	-	52.49	47.51	-	100	-	100
16 % In-TiO_2	100	-	100	-	100	-	100	-	63.73	36.27	-	100	-	100

*A= Anatase; R = Rutile

Raman spectroscopy:

Raman spectra of TiO_2 anatase (0 % In-TiO_2 @ 500 °C), TiO_2 rutile (0 % In-TiO_2 @ 700 °C) and In-TiO_2 samples (at 750 °C and 800 °C) are shown in Fig. 9. Raman modes of TiO_2 anatase such as E_g, B_{1g}, A_{1g} or B_{1g} and E_g are noted around 135.11 cm^{-1}, 390.36 cm^{-1}, 510.65 cm^{-1} and 632.54 cm^{-1}, respectively [25, 39]. The distinctive Raman modes of TiO_2 rutile such as B_{2g} and $3E_g$ are observed around 439.98 cm^{-1} and 602.94 cm^{-1}, respectively [25, 39]. The anatase peaks of In-TiO_2 are slightly blue-shifted, as compared to pure TiO_2. This is ascribed to the generation of defects and oxygen vacancies in TiO_2 by In doping [73, 74]. The bond between O-Ti-O is modified by In doping in the crystal lattice of TiO_2 [73]. It is also suggested that a high concentration of In^{3+} may induce a stress in the TiO_2 framework [70]. This is also evidenced by the variations in the average crystallite size from the XRD results. Raman peaks In_2O_3 are not clearly differentiated in the In-TiO_2 samples. This is ascribed to the low concentration of In and the peaks of In_2O_3 (*e.g.* 133 cm^{-1} - stretching vibration of In-O bond of InO_6 unit) are coincided well with the TiO_2 anatase peaks (E_g at 135.11 cm^{-1}) [75, 76].

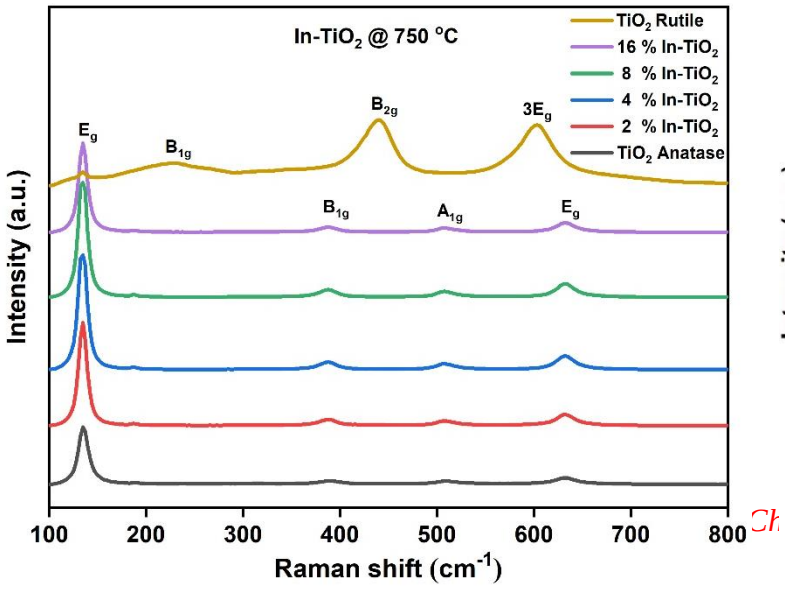

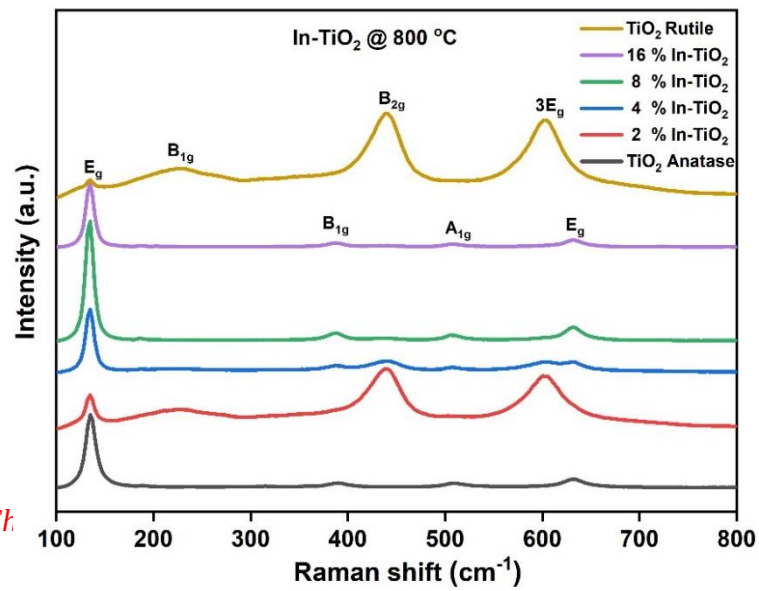

Fig. 9. Raman spectra of In-TiO_2 samples at (a) 750 °C and (b) 800 °C

Moreover, the variations in Raman peak intensity and area perfectly endorse the differences in anatase and rutile TiO_2 percentages (Table 1) by In doping.

X-ray photoelectron spectroscopy (XPS):

The chemical oxidation states of the elements in In-TiO_2 are examined by XPS and the results are displayed in Fig. 10. The survey spectrum of 16 % In-TiO_2 (800 °C) is displayed in Fig. 10 (a). The peaks of oxygen, titanium and indium are clearly noted at their corresponding binding energies. As shown in Fig. 10 (b), the electron binding energies of Ti $2p_{3/2}$ and Ti $2p_{1/2}$ are observed at 458.78 eV and 464.45 eV respectively, suggesting titanium is in +4 oxidation state (Ti^{4+}) [46]. There are no peaks observed for Ti^{3+} and Ti^{2+} states. The electronegativity of In^{3+} (1.78) is higher than that of Ti^{4+} (1.54), which may cause an electron transfer from Ti^{4+} and O^{2-} to In^{3+} [69]. This kind of electron transfer could make an electron deficiency in Ti^{4+} and O^{2-} and therefore the binding energies of Ti 2*p* and O 1*s* are increased. Moreover, In ions may be doped into TiO_2 crystal lattice through substitutional mode (*i.e.* lattice metal ions are substituted by the dopant metal ions) because the ionic radius of In^{3+} (0.08 nm) is higher than that of Ti^{4+} (0.06 nm)[47]. Therefore, new energy levels could be incorporated below the CB of TiO_2 *via* In doping [77, 78]. O 1*s* spectrum of In-TiO_2 is comprised of three component peaks at 530.01 eV, 531.62 eV and 532.32 eV, respectively. The main peak at 530.01 eV is ascribed to lattice oxygen (O^{2-}) in TiO_2. The additional peaks at 531.62 eV and 532.32 eV are attributed to In-O and surface free hydroxyl groups, respectively [69, 72]. Fig 10 (e) clearly shows that the impact of In dopant concentration on the surface hydroxyl groups and oxygen vacancies of TiO_2 crystal lattice. The presence of more surface hydroxyl groups is favourable to improving the photocatalytic activity [46] through the formation of hydroxyl radicals. In^{3+} peaks for In $3d_{5/2}$ and In $3d_{3/2}$ are observed at 444.74 eV and 452.29 eV (Fig. 10 (d)), respectively [74], indicating In is existed in the form of indium oxide. Fig 10 (f) shows that the binding energy values of In 3*d* peaks are decreased with increase of In dopant concentration. The existence of a small C 1*s* peak is attributed to adventitious carbon from the synthesis and calcination processes [72].

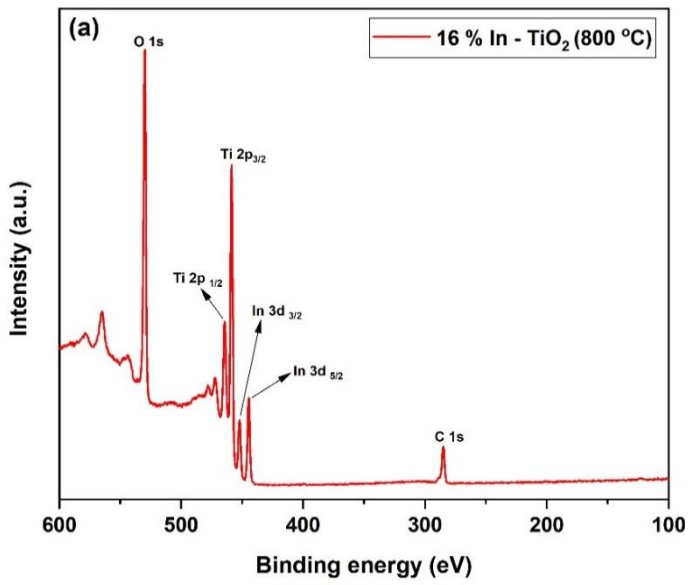
(a)
16 % In - TiO2 (800 °C)
O 1s
Ti 2p3/2
Ti 2p 1/2
In 3d 3/2
In 3d 5/2
C 1s
Intensity (a.u.)
Binding energy (eV)

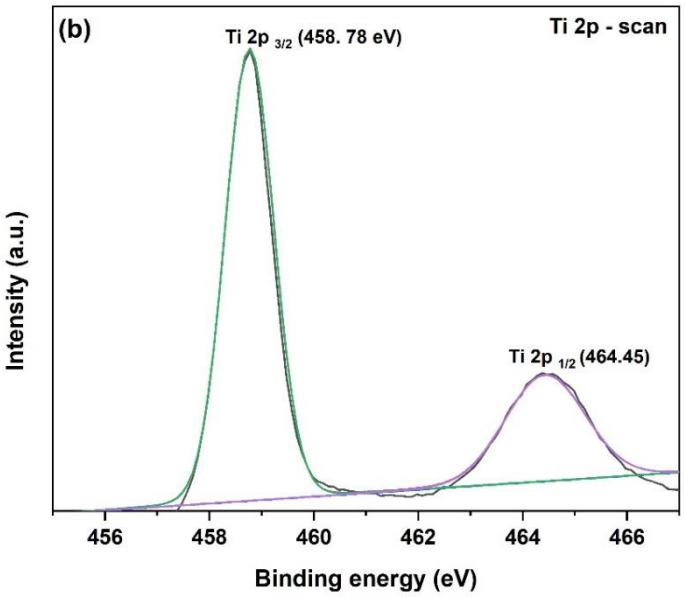
(b)
Ti 2p - scan
Ti 2p 3/2 (458. 78 eV)
Ti 2p 1/2 (464.45)
Intensity (a.u.)
Binding energy (eV)

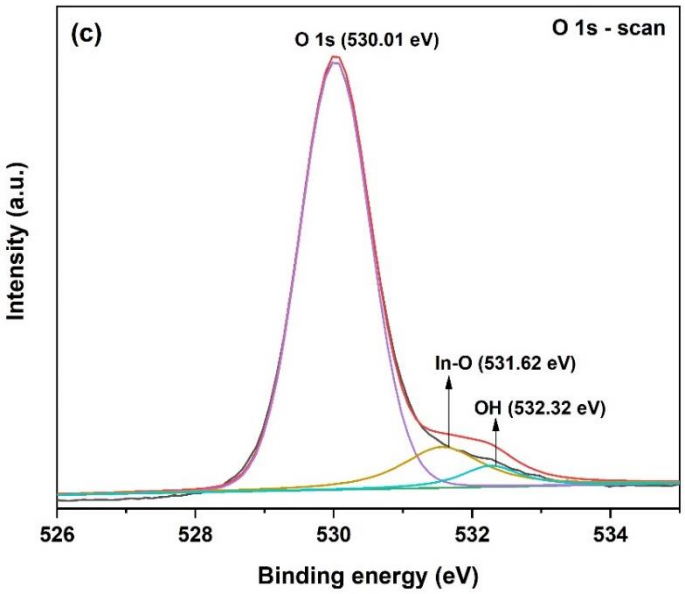
(c)
O 1s - scan
O 1s (530.01 eV)
In-O (531.62 eV)
OH (532.32 eV)
Intensity (a.u.)
Binding energy (eV)

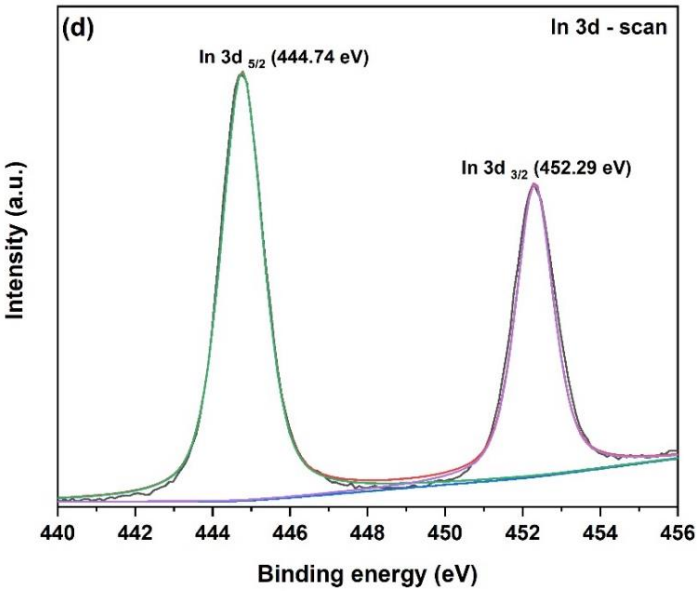
(d)
In 3d - scan
In 3d 5/2 (444.74 eV)
In 3d 3/2 (452.29 eV)
Intensity (a.u.)
Binding energy (eV)

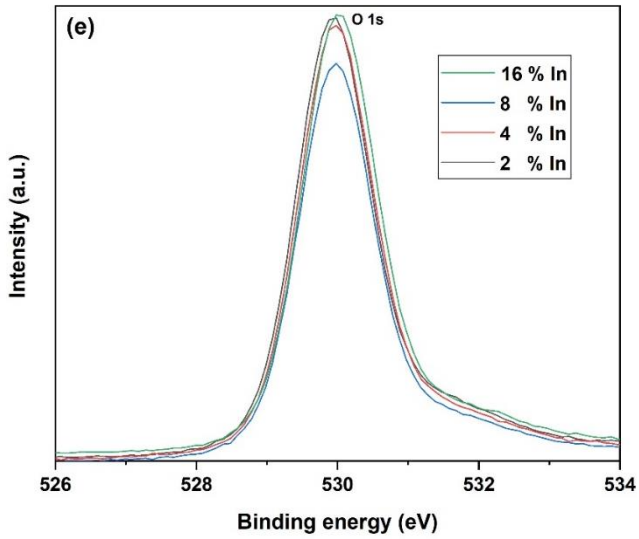
(e)
O 1s
16 % In
8 % In
4 % In
2 % In
Intensity (a.u.)
Binding energy (eV)

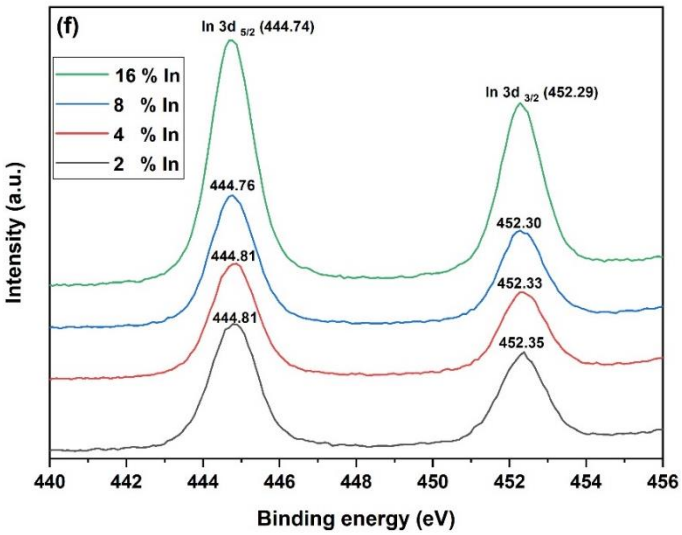
(f)
In 3d 5/2 (444.74)
In 3d 3/2 (452.29)
16 % In
8 % In
4 % In
2 % In
444.76
444.81
444.81
452.30
452.33
452.35
Intensity (a.u.)
Binding energy (eV)

Fig. 10. XPS spectra of In-TiO_2 at 800 °C (a) survey spectrum (b) Ti 2*p* (c) O 1*s* (d) In 3*d* (e) O 1*s* of 2, 4, 8 and 16 % In-TiO_2 (f) In 3*d* of 2, 4, 8 and 16 % In-TiO_2

Photoluminescence (PL):

PL spectra of pure TiO_2 anatase (0 % In-TiO_2 @ 500 °C) and In-TiO_2 (800 °C) are shown in Fig. 11. PL emission spectra are accredited to the recombination of electron-holes *via* a non-irradiative process inside TiO_2 [47]. PL signals are mainly attributed to the existence of surface states and defects [74]. The peaks noticed at 461 nm are associated with TiO_2 anatase [46, 68]. A peak noted at 423 nm is related to the formation of oxygen vacancies in TiO_2 during In doping. The peaks observed at 485 nm and 527 nm are ascribed to the transition of electrons (two trapped and one trapped) from the oxygen vacancies to the VB of TiO_2 [47].

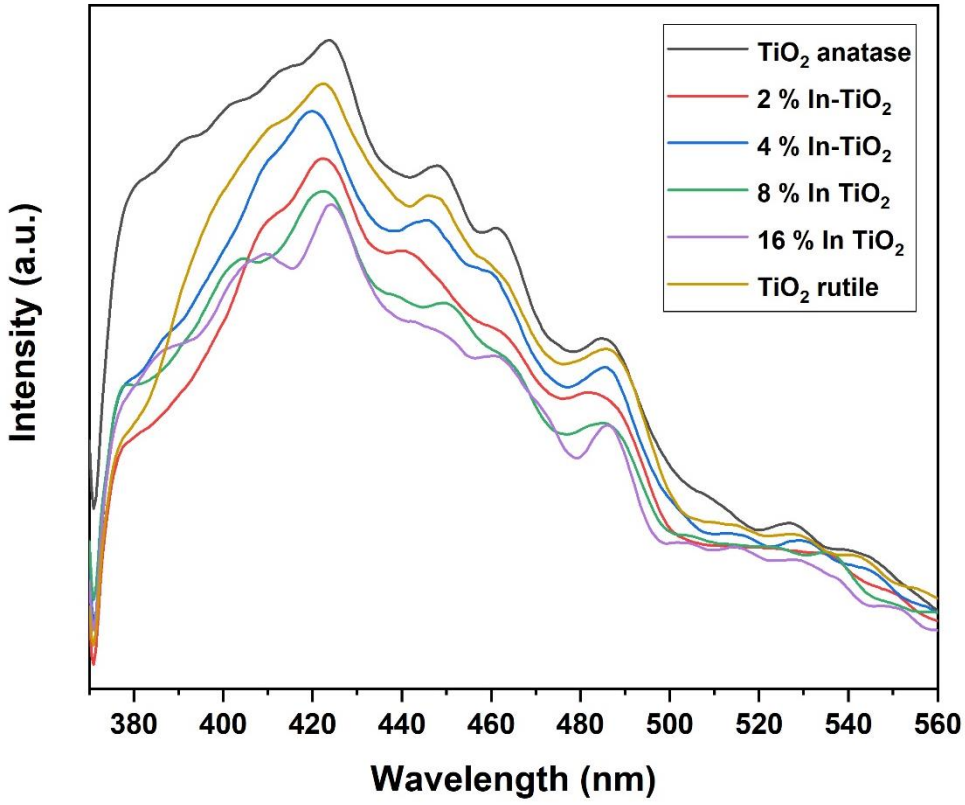

Fig. 11. PL spectra of TiO_2 anatase, TiO_2 rutile and In-TiO_2 samples

The energy of levels of two oxygen vacancies are positioned around 0.51 eV and 0.82 eV [47]. For the electron-hole recombination process, the photo-generated electrons could be transferred first from the CB to the oxygen vacancies (non- radiative process) and then to the VB (fluorescence emission) of TiO_2. Fig 11 shows that the emission intensity of PL peaks is significantly decreased with an increase in In dopant concentration. This indicates that the transition of electrons from the CB of TiO_2 to the oxygen vacancies is suppressed by the

creation of new energy levels through In doping. The surface state energy level of In might be positioned between the CB of TiO_2 and energy level of oxygen vacancies [47]. The formation of In-derived states in the band gap is consistent with the results from the DFT+U calculations showing In 5*s* states between the VB and CB of TiO_2. PL results show that the photo-generated electron hole recombination process on TiO_2 can be effectively suppressed by In doping, leading to a higher photocatalytic activity [68, 75, 79].

Photocurrent response analysis:

PL results were further supported by the transient photocurrent measurements. Fig. 12 (a) shows the transient photocurrent response of anatase, rutile and In-TiO_2 samples at +1.0 V vs SCE. Upon irradiation of the TiO_2 electrode, a significant increase in the anodic current was observed due to the photoexcitation of electrons to the conduction band. The difference in current of the TiO_2 working electrode between dark and light conditions is termed as photocurrent. The anodic photocurrent observed on nano-particulate electrodes is due to the diffusion of majority charge carriers through the particulate film to the supporting contact electrode. The current-time response is shown in Fig. 12 (a) under chopped irradiation. The steady-state photocurrent densities from the samples at +1.0 V are shown in Fig. 12 (b). The photocurrent densities of most of the In-TiO_2 samples are higher than that of anatase and rutile electrodes. This correlates with the DFT studies whereby new intra-band gap states due to In doping give rise to a greater charge carrier density under irradiation and therefore improved anodic photocurrent. The best photocurrent density is observed with the 16 % In-TiO_2 annealed at 800 ^oC. The photocurrent density of 8 % In-TiO_2 annealed at 800 ^oC is much lower than the other samples. This may be ascribed to the similar percentages of anatase (52.49 %) and rutile (47.51 %).

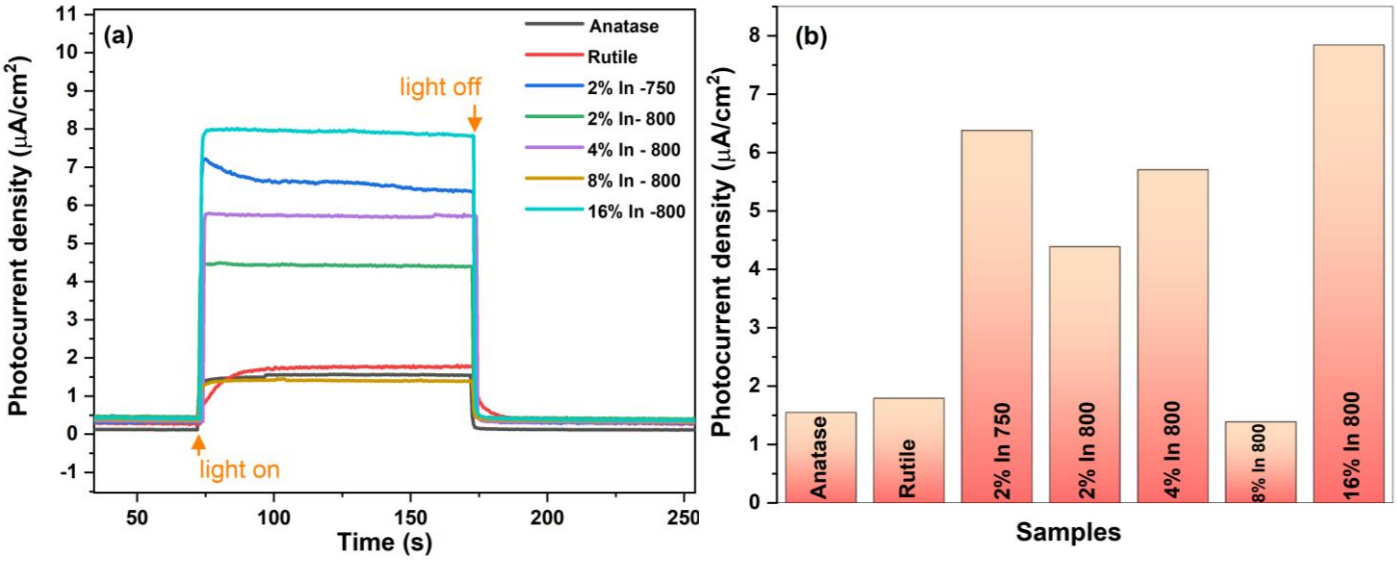

Fig. 12. (a) The photocurrent density of anatase, rutile and various In-TiO_2 samples at +1.0 V *vs* SCE, and (b) steady state photocurrent density of anatase, rutile and various In-TiO_2 samples at +1.0 V.

Photocatalytic H_2 production:

The samples were tested for photocatalytic H_2 production efficiency *via* water splitting under simulated solar light irradiation. H_2 production efficiency of 2 % In-TiO_2 @ 700 °C, 2 % In-TiO_2 @ 750 °C, 4 % In-TiO_2 @ 750 °C and 16 % In-TiO_2 @ 800 °C are shown in Fig. 13. H_2 production efficiency order of In-TiO_2 samples is 2 % In-TiO_2 @700 °C (105.2 µL of H_2/h) > 4 % In-TiO_2 @750 °C (31.5 µL of H_2/h) > 2 % In-TiO_2 @750 °C (28.2 µL of H_2/h) > 16 % In-TiO_2 @800 °C (25.6 µL of H_2/h) > 2 % In-TiO_2 @850 °C (19.20 µL of H_2/h). The efficiency of pure anatase and rutile were 145.6 µL of H_2/h and 65.4 µL of H_2/h, respectively. The photocatalytic activity of 2 % In-TiO_2 @700 °C is more comparable with that of pure anatase (0 % In-TiO_2 @500 °C). Nevertheless, the efficiency of In-TiO_2 is strongly influenced by the anatase percentage, calcination temperature and In concentration. The water splitting efficiency of TiO_2 is decreased with increasing of In content. This is ascribed to poor dispersion, agglomeration, and decrease of active surface area at high In content [80, 81]. It is also noticed that the colour of nanoparticles was changed from white to black during 6 h of light irradiation. This is accredited to the photo-reduction of In(III) to In(I) or In(0), indicating the poisoning of catalyst surface under prolonged light irradiation. The excess of In dopant could act also as an electron-hole recombination centre near the CB of TiO_2 [80]. It could be rectified with the help of a suitable co-catalyst [82]. There are no detailed studies for the water splitting efficiency of In-TiO_2 samples. In a recent study, the similar kind of trend was observed by Zhong *et al.*[80] for In doped barium titanate (In-$BaTiO_3$). The efficiency of In-$BaTiO_3$ was further improved with the help of cadmium selenide co-catalyst. However, the efficiency was again dropped when the In concentration was more than 2 %.

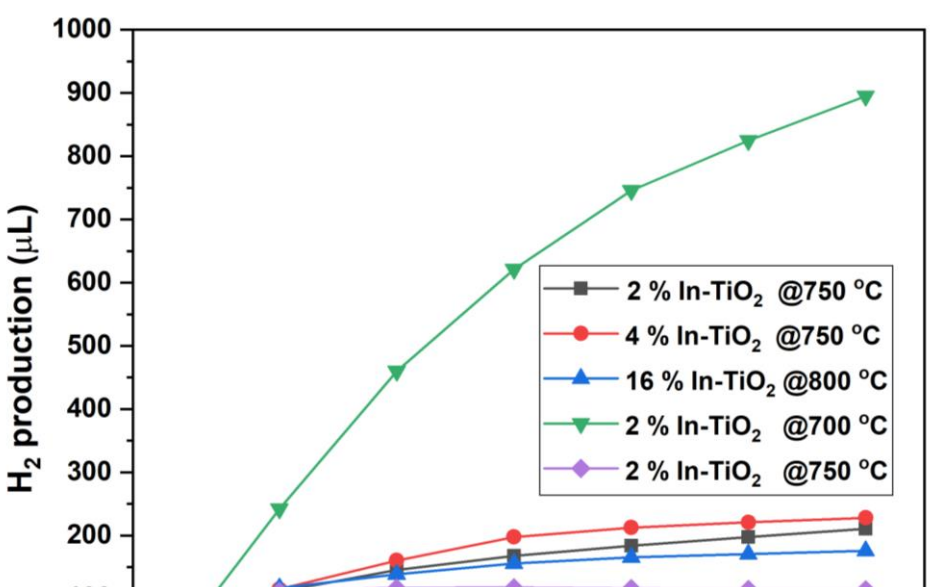

Fig. 13. H_2 production efficiency of 0.5 g/L of In-TiO_2 under simulated solar light irradiation

XRD, Raman, PL and photocurrent results verified DFT calculations for the generation of gap states (In- 5*s* states), variations in crystal lattice parameters and oxygen vacancies. DFT calculations also demonstrate the influence of In_2O_3 formation on anatase through the In_4O_6-a101 model. XRD results confirmed that the lattice parameters and cell volume of anatase are not significantly influenced by In doping. The variations in the anatase and rutile percentages for In-TiO_2 samples are endorsed by the differences in E_g and B_{2g} peaks in the Raman spectra. The increase in the lifetime of charge carriers after In doping is supported through PL and photocurrent analyses. The transition of electrons between oxygen vacancies and In energy levels is evidenced by the PL spectra. In dopant could improve the current density of TiO_2 and enhance the separation of charge carriers on the photocatalyst surface. During the photo-absorption phenomena, two electronic transitions are possible: (i) from the VB of TiO_2 to CB; (ii) from the VB of TiO_2 to In- 5*s* state [48]. This kind of electron transfer could favourably separate the photo-generated electron-hole pairs and increase their life time on the catalyst surface [74]. Besides, the Bronsted acidity of In-TiO_2 surface could further promote the adsorption of pollutant/microbes and H_3O^+/OH^- species to enhance the production of hydroxyl radicals [71]. Hinojosa-Reyes *et al.* [70] suggested that In dopant could also act as discrete reactive sites to accelerate the adsorption of pollutant on the photocatalyst surface. They found that In-TiO_2 coated perlite-granules showed the highest efficiency for the photochemical decomposition of ethylbenzene in contrast to pure TiO_2. The decrease of average crystallite size from the XRD results reveals the stabilization of TiO_2 anatase phase by In dopant during calcination [74]. It was evidenced that the small particle size of In-TiO_2 is beneficial to enhance the photocatalytic activity as compared to pure TiO_2 [42]. DFT results describe that the substitutional doping of In in the TiO_2 anatase crystal restricts the bond breaking and reformation to avoid the ART at high temperature [23]. Some studies suggested that In dopant on TiO_2 could also act as an electron trap to stimulate the electron transfer to surface adsorbed oxygen for the generation of reactive oxygen species [42, 68]. Even though, a

high concentration of In could preserve the anatase content (more than 700 °C calcination temperature) in this present work, the water splitting efficiency is influenced by the concentration of In [83]. This is accredited to the poor bonding interactions between In-TiO_2, water and glycerol, which could reduce the dispersion of nanoparticles in water [81]. A high concentration of In leads to the formation of In_2O_3, which could reduce the interface area between the dopant and TiO_2. In addition to that, a thin layer of In_2O_3 could cover the reactive sites of TiO_2 responsible for water splitting [84]. The high grain size of In-TiO_2 (samples at high calcination temperature) affects the mass transport and accessibility of the reactants at the photocatalyst surface [83]. H_2 production efficiency of 2 % In-TiO_2 calcined at 700 °C is more comparable with respect to pure anatase (0 % In-TiO_2 calcined at 500 °C) and it could be used as a thermally stable photocatalytic coating. Future studies should be focused to improve the dispersion of In-TiO_2 calcined at high temperatures.

4. Conclusions:

The effect of indium doping on the anatase rutile transition of TiO_2 was systematically studied in a temperature range of 500 °C – 900 °C. Theoretical and experimental characterizations were performed for the as-synthesised In-TiO_2 nanoparticles. The results shown that In is an effective dopant to preserve the anatase content of TiO_2, up to 64 % at a temperature as high as 800 °C. The ART of TiO_2 is strongly influenced by the In dopant concentration. XRD results revealed that In^{3+} retards the crystallization of TiO_2 through the substitution of Ti^{4+} ions. Raman spectroscopy shows the generation of defects and oxygen vacancies in TiO_2 by In doping. The lifetime of photo-generated charge carriers in TiO_2 could also be extended by In doping.

DFT results indicate that charge compensating oxygen vacancies will form spontaneously in In-doped TiO_2 and that formation of further, reducing oxygen vacancies have moderate energy costs. Considerations of oxygen vacancy formation as the primary mechanism in the ART is therefore insufficient in accounting for the inhibition of the transition reported in the experimental findings. The computed DOS plots for In-doped bulk anatase TiO_2 reveal that, upon formation of reducing oxygen vacancies, states emerge in the bandgap due to localisation of charge in the vicinity of the In-dopants.

Our model for In_2O_3 formation at the anatase (101) surface indicates that the In_4O_6 nanocluster is bound at the surface with a moderate adsorption energy. We predict that for higher calcination temperatures the In_2O_3 at the surface will desorb or migrate and aggregate

at the surface. The latter outcome would explain the enhanced In_2O_3 signals in the XRD spectrum for those samples calcined at higher temperatures. Formation of a reducing oxygen vacancy in the surface bound In_2O_3 has moderate formation energies with the resulting excess charge localizing at In sites are the surface. The presence of In_2O_3 at the surface extends the VBM of the titania support to higher energies and, in combination with In-derived states in the bandgap for both stoichiometric and reduced In_2O_3, a red shift in the light absorption edge is predicted.

The photocatalytic activity of 2 % In-TiO_2 @700 °C is more similar with that of pure anatase. It could be further improved with the help of appropriate co-catalyst. The photocatalytic activity is strongly affected by the calcination temperature and anatase percentage. Overall, the results demonstrate that In is an effective dopant for the fabrication of thermally stable TiO_2 with photocatalytic activity.

Acknowledgements:

The authors are grateful to the Renewable Engine project funded by European Union's INTERREG VA Programme, managed by the Special EU Programmes Body (SEUPB), with match funding provided by the Department for the Economy and Department of Jobs, Enterprise and Innovation in Ireland. SR and MN acknowledge the support from Science Foundation Ireland through the ERA. Net for Materials Research and Innovation (M-ERA.Net 2), Horizon 2020 grant agreement number 685451, SFI Grant Number SFI/16/M-ERA/3418 (RATOCAT). We acknowledge access to SFI funded computing resources at Tyndall Institute and the SFI/HEA funded Irish Centre for High End Computing. We are grateful for support from the COST Action CM1104 "Reducible Metal Oxides, Structure and Function". AS would like to acknowledge the financial support via VCRS scholarship from Ulster University. PKS and TB would like to acknowledge Invest Northern Ireland for financial assistance (R&D project Novel Dielectrics RD071392).

References:

1. Kogo, A.; Sanehira, Y.; Numata, Y.; Ikegami, M.; Miyasaka, T., Amorphous Metal Oxide Blocking Layers for Highly Efficient Low-Temperature Brookite TiO_2-Based Perovskite Solar Cells. *ACS Appl. Mater. Interfaces* **2018**, *10*, 2224-2229.
2. Huang, J.; Li, G.; Zhou, Z.; Jiang, Y.; Hu, Q.; Xue, C.; Guo, W., Efficient Photocatalytic Hydrogen Production over Rh and Nb Codoped TiO_2 Nanorods. *Chem. Eng. J.* **2018**, *337*, 282-289.
3. Low, J.; Qiu, S.; Xu, D.; Jiang, C.; Cheng, B., Direct Evidence and Enhancement of Surface Plasmon Resonance Effect on Ag-Loaded TiO_2 Nanotube Arrays for Photocatalytic CO_2 Reduction. *Appl. Surf. Sci*. **2018**, *434*, 423-432.
4. Ganguly, P.; Byrne, C.; Breen, A.; Pillai, S. C., Antimicrobial Activity of Photocatalysts: Fundamentals, Mechanisms, Kinetics and Recent Advances. *Appl. Catal., B* **2018,** *225*, 51-75.
5. Hazarika, D.; Saikia, D.; Gupta, K.; Mandal, M.; Karak, N., Photoluminescence, Self Cleaning and Photocatalytic Behavior of Waterborne Hyperbranched Polyester/Carbon Dot@ TiO_2 Nanocomposite. *Chemistry Select* **2018**, *3*, 6126-6135.
6. Lyulyukin, M.; Kolinko, P.; Selishchev, D.; Kozlov, D., Hygienic Aspects of TiO_2-Mediated Photocatalytic Oxidation of Volatile Organic Compounds: Air Purification Analysis Using a Total Hazard Index. *Appl. Catal., B* **2018**, *220*, 386-396.
7. Pastrana-Martínez, L. M.; Morales-Torres, S.; Carabineiro, S. A.; Buijnsters, J. G.; Figueiredo, J. L.; Silva, A. M.; Faria, J. L., Photocatalytic Activity of Functionalized Nanodiamond-TiO_2 Composites Towards Water Pollutants Degradation under UV/Vis Irradiation. *Appl. Surf. Sci*. **2018**, *458*, 839-848..
8. Kumaravel, V.; Mathew, S.; Bartlett, J.; Pillai, S. C., Photocatalytic Hydrogen Production Using Metal Doped TiO_2: A Review of Recent Advances. *Appl. Catal., B* **2019,** *244*, 1021-1064.
9. Li, Y.; Lv, K.; Ho, W.; Dong, F.; Wu, X.; Xia, Y., Hybridization of Rutile TiO_2 (Rt-TiO_2) with g-C_3N_4 Quantum Dots (CN Qds): An Efficient Visible-Light-Driven Z-Scheme Hybridized Photocatalyst. *Appl. Catal., B* **2017**, *202*, 611-619.
10. Boningari, T.; Inturi, S. N. R.; Suidan, M.; Smirniotis, P. G., Novel one-step synthesis of sulfur doped-TiO_2 by flame spray pyrolysis for visible light photocatalytic degradation of acetaldehyde. *Chem. Eng. J.* **2018,** *339*, 249-258.
11. Vignesh, K.; Suganthi, A.; Rajarajan, M.; Sakthivadivel, R., Visible Light Assisted Photodecolorization of Eosin-Y in Aqueous Solution Using Hesperidin Modified TiO_2 Nanoparticles. *Appl. Surf. Sci*. **2012**, *258*, 4592-4600.
12. Moradi, V.; Jun, M. B.; Blackburn, A.; Herring, R. A., Significant Improvement in Visible Light Photocatalytic Activity of Fe Doped TiO_2 Using an Acid Treatment Process. *Appl. Surf. Sci*. **2018**, *427*, 791-799.
13. Vignesh, K.; Priyanka, R.; Hariharan, R.; Rajarajan, M.; Suganthi, A., Fabrication of CdS and $CuWO_4$ Modified TiO_2 Nanoparticles and Its Photocatalytic Activity under Visible Light Irradiation. *J. Ind. Eng. Chem*. **2014**, *20*, 435-443.
14. Li, J.; Zhang, M.; Li, Q.; Yang, J., Enhanced Visible Light Activity on Direct Contact Z-Scheme G-C_3N_4-TiO_2 Photocatalyst. *Appl. Surf. Sci*. **2017**, *391*, 184-193.
15. Liu, L.; Zhao, H.; Andino, J. M.; Li, Y., Photocatalytic CO_2 Reduction with H_2O on TiO_2 Nanocrystals: Comparison of Anatase, Rutile, and Brookite Polymorphs and Exploration of Surface Chemistry. *ACS Catal*. **2012**, *2*, 1817-1828.
16. Zhang, J.; Zhou, P.; Liu, J.; Yu, J., New Understanding of the Difference of Photocatalytic Activity among Anatase, Rutile and Brookite TiO_2. *Phys. Chem. Chem. Phys*. **2014**, *16*, 20382-20386.

17. Koltsakidou, A.; Antonopoulou, M.; Evgenidou, E.; Konstantinou, I.; Giannakas, A.; Papadaki, M.; Bikiaris, D.; Lambropoulou, D., Photocatalytical Removal of Fluorouracil Using TiO_2-P25 and N/S Doped TiO_2 Catalysts: A Kinetic and Mechanistic Study. *Sci. Total Environ.* **2017**, *578*, 257-267.
18. Shayegan, Z.; Haghighat, F.; Lee, C.-S.; Bahloul, A.; Huard, M., Effect of Surface Fluorination of P25-TiO_2 on Adsorption of Indoor Environment Volatile Organic Compounds. *Chem. Eng. J.* **2018**, *346*, 578-589.
19. Mohamed, M. A.; Salleh, W.; Jaafar, J.; Ismail, A.; Nor, N. A. M.; Physics, Photodegradation of Phenol by N-Doped TiO_2 Anatase/Rutile Nanorods Assembled Microsphere under Uv and Visible Light Irradiation. *Mater. Chem. Phys.* **2015**, *162*, 113-123.
20. Fagan, R.; Synnott, D. W.; McCormack, D. E.; Pillai, S. C., An Effective Method for the Preparation of High Temperature Stable Anatase TiO_2 Photocatalysts. *Appl. Surf. Sci.* **2016**, *371*, 447-452.
21. Bossa, N.; Chaurand, P.; Levard, C.; Borschneck, D.; Miche, H.; Vicente, J.; Geantet, C.; Aguerre-Chariol, O.; Michel, F. M.; Rose, J., Environmental Exposure to TiO_2 Nanomaterials Incorporated in Building Material. *Environ. Pollut.* **2017**, *220*, 1160-1170.
22. Lin, C.-C.; Chen, W.-Y., Effect of Paint Composition, Nano-Metal Types and Substrate on the Improvement of Biological Resistance on Paint Finished Building Material. *Build. Environ.* **2017**, *117*, 49-59.
23. Hanaor, D. A.; Sorrell, C. C., Review of the Anatase to Rutile Phase Transformation. *J. Mater. Sci.* **2011**, *46*, 855-874.
24. Ding, K.; Miao, Z.; Hu, B.; An, G.; Sun, Z.; Han, B.; Liu, Z., Study on the Anatase to Rutile Phase Transformation and Controlled Synthesis of Rutile Nanocrystals with the Assistance of Ionic Liquid. *Langmuir* **2010**, *26*, 10294-10302.
25. Byrne, C.; Fagan, R.; Hinder, S.; McCormack, D. E.; Pillai, S. C., New Approach of Modifying the Anatase to Rutile Transition Temperature in TiO_2 Photocatalysts. *RSC Adv.* ***2016***, *6*, *95232-95238.*
26. Wang, C.-L.; Hwang, W.-S.; Chu, H.-L.; Lin, H.-J.; Ko, H.-H.; Wang, M.-C., Kinetics of Anatase Transition to Rutile TiO_2 from Titanium Dioxide Precursor Powders Synthesized by a Sol-Gel Process. *Ceram. Int.* **2016**, *42*, 13136-13143.
27. Khatun, N.; Tiwari, S.; Lal, J.; Tseng, C.-M.; Liu, S. W.; Biring, S.; Sen, S., Stabilization of Anatase Phase by Uncompensated Ga-V Co-Doping in TiO_2: A Structural Phase Transition, Grain Growth and Optical Property Study. *Ceram. Int.* **2018**, *44*, 22445-22455.
28. Nguyen, C.-C.; Nguyen, D. T.; Do, T.-O., A Novel Route to Synthesize C/Pt/TiO_2 Phase Tunable Anatase–Rutile TiO2 for Efficient Sunlight-Driven Photocatalytic Applications. *Appl. Catal., B* **2018**, *226*, 46-52.
29. Potlog, T.; Dobromir, M.; Luca, D.; Onufrijevs, P.; Medvids, A.; Shamardin, A., Rutile to Anatase Phase Transition in TiO_2: Nb Thin Films by Annealing in H_2 Atmosphere. *Curr. Appl. Phys.* **2016**, *16*, 826-829.
30. Mathew, S.; Ganguly, P.; Rhatigan, S.; Kumaravel, V.; Byrne, C.; Hinder, S.; Bartlett, J.; Nolan, M.; Pillai, S., Cu-Doped TiO_2: Visible Light Assisted Photocatalytic Antimicrobial Activity. *Appl. Sci.* **2018**, *8*, 2067.
31. Huang, F.; Motealleh, B.; Zheng, W.; Janish, M. T.; Carter, C. B.; Cornelius, C. J., Electrospinning Amorphous SiO_2-TiO_2 and TiO_2 Nanofibers Using Sol-Gel Chemistry and Its Thermal Conversion into Anatase and Rutile. *Ceram. Int.* **2018**, *44*, 4577-4585.
32. Tsai, C.-M.; Song, C.-G.; Hung, Y.-C.; Jeong, Y.-G.; Oh, S. H.; Jeong, J. H.; Kim, H.; Huh, H.; Yoon, J.-W.; Sigmund, W., Carbon Induced Phase Transformation in Electrospun Tio2/Multiwall Carbon Nanotube Nanofibers. *Ceram. Int.* **2017**, *43*, 3761-3768.

33. Da Silva, A. L.; Dondi, M.; Hotza, D., Self-Cleaning Ceramic Tiles Coated with Nb_2O_5-Doped-TiO_2 Nanoparticles. *Ceram. Int.* **2017**, *43*, 11986-11991.
34. Khatun, N.; Tiwari, S.; Lal, J.; Tseng, C.-M.; Liu, S. W.; Biring, S.; Sen, S., Stabilization of Anatase Phase by Uncompensated Ga-V Co-Doping in TiO_2: A Structural Phase Transition, Grain Growth and Optical Property Study. *Ceram. Int.* **2018**, *44*, 22445-22455.
35. Li, J.; Xu, X.; Liu, X.; Qin, W.; Pan, L., Novel Cake-Like N-Doped Anatase/Rutile Mixed Phase TiO_2 Derived from Metal-Organic Frameworks for Visible Light Photocatalysis. *Ceram. Int.* **2017**, *43*, 835-840.
36. Giraldi, T. R.; Dias, J. A.; Baggio, C. M.; Maestrelli, S. C.; Oliveira, J. A., Anatase-to-Rutile Transition in Co-Doped TiO_2 Pigments. *J. Sol-Gel Sci. Technol.* **2017**, *83*, 115-123.
37. Yadav, A. K.; Khatun, N.; Kumar, S.; Tseng, C.-M.; Biring, S.; Sen, S. , Size and Strain Dependent Anatase to Rutile Phase Transition in TiO_2 Due to Si Incorporation. *J. Mater. Sci.- Mater. Electron.* **2017**, *28*, 19017-19024.
38. Kondamareddy, K. K.; Neena, D.; Lu, D.; Peng, T.; Lopez, M. A. M.; Wang, C.; Yu, Z.; Cheng, N.; Fu, D.; Zhao, X.-Z., Ultra-Trace (Parts Per Million-Ppm) W^{6+} Dopant Ions Induced Anatase to Rutile Transition (ART) of Phase Pure Anatase TiO_2 Nanoparticles for Highly Efficient Visible Light-Active Photocatalytic Degradation of Organic Pollutants. *Appl. Surf. Sci.* **2018,** *456*, 676-693.
39. Khatun, N.; Rajput, P.; Bhattacharya, D.; Jha, S.; Biring, S.; Sen, S., Anatase to Rutile Phase Transition Promoted by Vanadium Substitution in TiO_2: A Structural, Vibrational and Optoelectronic Study. *Ceram. Int.* **2017**, *43*, 14128-14134.
40. Makal, P.; Das, D., Self-Doped TiO_2 Nanowires in TiO_2-B Single Phase, TiO2-B/Anatase and TiO2-Anatase/Rutile Heterojunctions Demonstrating Individual Superiority in Photocatalytic Activity under Visible and UV Light. *Appl. Surf. Sci.* **2018**, *455*, 1106-1115.
41. Reddy, B. M.; Sreekanth, P. M.; Reddy, E. P.; Yamada, Y.; Xu, Q.; Sakurai, H.; Kobayashi, T., Surface Characterization of La_2O_3− TiO_2 and V_2O_5/La_2O_3− TiO_2 Catalysts. *J. Phys. Chem. B* **2002**, *106*, 5695-5700.
42. Tahir, M.; Amin, N. S., Photocatalytic CO_2 Reduction and Kinetic Study over in/TiO2 Nanoparticles Supported Microchannel Monolith Photoreactor. *Appl. Catal., B* **2013**, *467*, 483-496.
43. Yu, Y.; Wang, E.; Yuan, J.; Cao, Y., Enhanced Photocatalytic Activity of Titania with Unique Surface Indium and Boron Species. *Appl. Surf. Sci.* **2013**, *273*, 638-644.
44. Zhang, Y.; Xu, H.; Xu, Y.; Zhang, H.; Wang, Y., The Effect of Lanthanide on the Degradation of Rb in Nanocrystalline Ln/TiO_2 Aqueous Solution. *J. Photochem. Photobiol., A* **2005**, *170*, 279-285.
45. Byrne, C.; Moran, L.; Hermosilla, D.; Merayo, N.; Blanco, Á.; Rhatigan, S.; Hinder, S.; Ganguly, P.; Nolan, M.; Pillai, S. C., Effect of Cu Doping on the Anatase-to-Rutile Phase Transition in TiO_2 Photocatalysts: Theory and Experiments. *Appl. Catal., B* **2019,** *246*, 266-276.
46. Tahir, M.; Amin, N. S., Indium-Doped TiO_2 Nanoparticles for Photocatalytic CO_2 Reduction with H2O Vapors to CH4. *Appl. Catal., A* **2015**, *162*, 98-109.
47. Wang, E.; Yang, W.; Cao, Y., Unique Surface Chemical Species on Indium Doped TiO2 and Their Effect on the Visible Light Photocatalytic Activity. *J. Phys. Chem. C* **2009**, *113*, 20912-20917.
48. Wang, E.; Zhang, P.; Chen, Y.; Liu, Z.; He, T.; Cao, Y., Improved Visible-Light Photocatalytic Activity of Titania Activated by Nitrogen and Indium Modification. *J. Phys. Chem. C* **2012**, *22*, 14443-14449.

49. Iwaszuk, A.; Nolan, M., Charge Compensation in Trivalent Cation Doped Bulk Rutile TiO_2. *J. Phys.: Condens. Matter* **2011**, *23*, 334207.
50. Khan, M.; Lan, Z.; Zeng, Y., Analysis of Indium Oxidation State on the Electronic Structure and Optical Properties of TiO_2. *Materials* **2018**, *11*, 952.
51. Kresse, G.; Furthmüller, J., Efficiency of Ab-Initio Total Energy Calculations for Metals and Semiconductors Using a Plane-Wave Basis Set. *Comput. Mater. Sci.* **1996**, *6*, 15-50.
52. Kresse, G.; Furthmüller, J., Efficient Iterative Schemes for Ab-Initio Total-Energy Calculations Using a Plane-Wave Basis Set. *Phys. Rev. B* **1996**, *54*, 11169.
53. Kresse, G.; Joubert, D., From Ultrasoft Pseudopotentials to the Projector Augmented-Wave Method. *Phys. Rev. B.* **1999**, *59*, 1758-1775.
54. Blöchl, P. E., Projector Augmented-Wave Method. *Phys. Rev. B.* **1994**, *50*, 17953-17979.
55. Anisimov, V. I.; Zaanen, J.; Andersen, O. K., Band Theory and Mott Insulators: Hubbard U Instead of Stoner I. *Phys. Rev. B.* **1991**, *44*, 943-954.
56. Dudarev, S. L.; Botton, G. A.; Savrasov, S. Y.; Humphreys, C. J.; Sutton, A. P., Electron-energy-loss spectra and the structural stability of nickel oxide: An LSDA+U study. *Phys. Rev. B.* **1998,** *57*, 1505-1509.
57. Carey, J. J.; Nolan, M., Dissociative adsorption of methane on the Cu and Zn doped (111) surface of CeO_2. *Appl. Catal., B* **2016,** *197*, 324-336.
58. Nolan, M.; Elliott, S. D., The p-type conduction mechanism in Cu_2O: a first principles study. *Phys. Chem. Chem. Phys.* **2006,** *8*, 5350-5358.
59. Morgan, B. J.; Watson, G. W., A DFT + U description of oxygen vacancies at the TiO_2 rutile (1 1 0) surface. *Surf. Sci.* **2007,** *601*, 5034-5041.
60. Nolan, M.; Elliott, S. D.; Mulley, J. S.; Bennett, R. A.; Basham, M.; Mulheran, P., Electronic structure of point defects in controlled self-doping of the TiO_2 (110) surface: Combined photoemission spectroscopy and density functional theory study. *Phys. Rev. B.* **2008,** *77*, 235424.
61. Kowalski, P. M.; Camellone, M. F.; Nair, N. N.; Meyer, B.; Marx, D., Charge Localization Dynamics Induced by Oxygen Vacancies on the TiO_2 Surface. *Phys. Rev. Lett.* **2010**, *105*, 146405.
62. Henkelman, G.; Arnaldsson, A.; Jónsson, H., A Fast and Robust Algorithm for Bader Decomposition of Charge Density. *Comput. Mater. Sci.* **2006**, *36*, 354-360.
63. Ilie, A. G.; Scarisoreanu, M.; Dutu, E.; Dumitrache, F.; Banici, A.-M.; Fleaca, C. T.; Vasile, E.; Mihailescu, I. J. A. S. S., Study of Phase Development and Thermal Stability in as Synthesized TiO_2 Nanoparticles by Laser Pyrolysis: Ethylene Uptake and Oxygen Enrichment. *Appl. Sur. Sci.* **2018**, *427*, 798-806.
64. Boningari, T.; Inturi, S. N. R.; Suidan, M.; Smirniotis, P. G., Novel One-Step Synthesis of Nitrogen-Doped TiO_2 by Flame Aerosol Technique for Visible-Light Photocatalysis: Effect of Synthesis Parameters and Secondary Nitrogen (N) Source. *Chem. Eng. J.* **2018**, *350*, 324-334.
65. Sharma, P. K.; Cortes, M. A. L.; Hamilton, J. W.; Han, Y.; Byrne, J. A.; Nolan, M., Surface modification of TiO_2 with copper clusters for band gap narrowing. *Catal. Today* **2019,** *321*, 9-17.
66. Pillai, S. C.; Periyat, P.; George, R.; McCormack, D. E.; Seery, M. K.; Hayden, H.; Colreavy, J.; Corr, D.; Hinder, S. J., Synthesis of high-temperature stable anatase TiO_2 photocatalyst. *J. Phys. Chem. C* **2007,** *111*, 1605-1611.
67. Fagan, R.; McCormack, D. E.; Hinder, S.; Pillai, S. C., Improved high temperature stability of anatase TiO_2 photocatalysts by N, F, P co-doping. *Mater. Des.* **2016,** *96*, 44-53.

68. Hamadanian, M.; Reisi-Vanani, A.; Razi, P.; Hoseinifard, S.; Jabbari, V., Photodeposition-assisted synthesis of novel nanoparticulate In, S-codoped TiO_2 powders with high visible light-driven photocatalytic activity. *Appl. Surf. Sci.* **2013,** *285*, 121-129.
69. Zhang, W.; Pei, X.; Chen, J.; He, H., Effects of Al doping on properties of xAl–3% In–TiO_2 photocatalyst prepared by a sol–gel method. *Mater. Sci. Semicond. Process.* **2015,** *38*, 24-30.
70. Hinojosa-Reyes, M.; Arriaga, S.; Diaz-Torres, L.; Rodríguez-González, V., Gas-Phase Photocatalytic Decomposition of Ethylbenzene over Perlite Granules Coated with Indium Doped TiO_2. *Chem. Eng. J.* **2013**, *224*, 106-113.
71. Myilsamy, M.; Mahalakshmi, M.; Murugesan, V.; Subha, N., Enhanced Photocatalytic Activity of Nitrogen and Indium Co-Doped Mesoporous TiO_2 Nanocomposites for the Degradation of 2, 4-Dinitrophenol under Visible Light. *Appl. Surf. Sci.* **2015**, *342*, 1-10.

72. Tahir, B.; Tahir, M.; Amin, N. S., Gold–Indium Modified TiO_2 Nanocatalysts for Photocatalytic CO2 Reduction with H2 as Reductant in a Monolith Photoreactor. *Appl. Sur. Sci.* **2015**, *338*, 1-14.
73. Choudhury, B.; Choudhury, A., Oxygen Vacancy and Dopant Concentration Dependent Magnetic Properties of Mn Doped TiO_2 Nanoparticle. *Curr. Appl. Phys.* **2013**, *13*, 1025-1031.
74. Sasikala, R.; Shirole, A.; Sudarsan, V.; Sudakar, C.; Naik, R.; Rao, R.; Bharadwaj, S., Enhanced Photocatalytic Activity of Indium and Nitrogen Co-Doped TiO_2–Pd Nanocomposites for Hydrogen Generation. *Appl. Catal., A* **2010**, *377*, 47-54.
75. Al mashary, F. S.; de Castro, S., et al., Effect of Growth Techniques on the Structural, Optical and Electrical Properties of Indium Doped TiO_2 Thin Films. *J. Alloys Compd.* **2018**, *766*, 194-203.
76. Al Saqri, N. A., et al., Investigation of Defects in Indium Doped TiO_2 Thin Films Using Electrical and Optical Techniques. *J. Alloys Compd*. **2017**, *698*, 883-891.
77. Yang, X.; Wang, Y.; Xu, L.; Yu, X.; Guo, Y. J. T., Silver and Indium Oxide Codoped TiO2 Nanocomposites with Enhanced Photocatalytic Activity. *J. Phys. Chem. C* **2008**, *112*, 11481-11489.
78. Sasikala, R.; Sudarsan, V.; Sudakar, C.; Naik, R.; Panicker, L.; Bharadwaj, S., Modification of the Photocatalytic Properties of Self Doped TiO_2 Nanoparticles for Hydrogen Generation Using Sunlight Type Radiation. *Int. J. Hydrogen Energy* **2009**, *34*, 6105-6113.
79. Beula, R. J.; Devadason, S.; Vidhya, B., Incorporation of Indium in TiO_2-Based Photoanodes for Enhancing the Photovoltaic Conversion Efficiency of Dye-Sensitized Solar Cells. *Appl. Nanosci*. **2018**, 1-9.

80. Zhong, D.; Liu, W.; Tan, P.; Zhu, A.; Qiao, L.; Bian, Y.; Pan, J., Efficient hydrogen generation of indium doped $BaTiO_3$ decorated with CdSe quantum dots: Novel understanding of the effect of doping strategy. *Int. J. Hydrogen Energy* **2019,** *44*, 1627-1639

81. Kumaravel, V.; Imam, M. D.; Badreldin, A.; Chava, R. K.; Do, J. Y.; Kang, M.; Abdel-Wahab, A., Photocatalytic Hydrogen Production: Role of Sacrificial Reagents on the Activity of Oxide, Carbon, and Sulfide Catalysts. *Catalysts* **2019,** *9*, 276.
82. Ganguly, P.; Harb, M.; Cao, Z.; Cavallo, L.; Breen, A.; Dervin, S.; Dionysiou, D. D.; Pillai, S. C., 2D Nanomaterials for Photocatalytic Hydrogen Production. *ACS Energy Lett.* **2019**, *4*, 1687-1709.

83. Xu, L.; Guan, J.; Shi, W.; Liu, L., Heterostructured mesoporous In_2O_3/Ta_2O_5 composite photocatalysts for hydrogen evolution: Impacts of In_2O_3 content and calcination temperature. *J. Colloid Interface Sci.* **2012,** *377*, 160-168.
84. Cao, S.-W.; Liu, X.-F.; Yuan, Y.-P.; Zhang, Z.-Y.; Liao, Y.-S.; Fang, J.; Loo, S. C. J.; Sum, T. C.; Xue, C., Solar-to-fuels conversion over In_2O_3/g-C_3N_4 hybrid photocatalysts. *Appl. Catal., B* **2014,** *147*, 940-946.